



A Hybrid Kinetic Model of Asymmetric Thin Current Sheets with Sheared Flows in a Collisionless Plasma

JAMES CHEN

*Beam Physics Branch
Plasma Physics Division*

ROBERT A. SANTORO

*NRC Postdoctoral Research Associate
Beam Physics Branch
Plasma Physics Division*

ADAM SZABO

*NASA Goddard Space Flight Center
Greenbelt, Maryland*

DAVIN E. LARSON

*Space Science Laboratory
University of California
Berkeley, California*

December 27, 2010

REPORT DOCUMENTATION PAGE

Form Approved
OMB No. 0704-0188

Public reporting burden for this collection of information is estimated to average 1 hour per response, including the time for reviewing instructions, searching existing data sources, gathering and maintaining the data needed, and completing and reviewing this collection of information. Send comments regarding this burden estimate or any other aspect of this collection of information, including suggestions for reducing this burden to Department of Defense, Washington Headquarters Services, Directorate for Information Operations and Reports (0704-0188), 1215 Jefferson Davis Highway, Suite 1204, Arlington, VA 22202-4302. Respondents should be aware that notwithstanding any other provision of law, no person shall be subject to any penalty for failing to comply with a collection of information if it does not display a currently valid OMB control number. **PLEASE DO NOT RETURN YOUR FORM TO THE ABOVE ADDRESS.**

1. REPORT DATE (DD-MM-YYYY) 27-12-2010		2. REPORT TYPE Interim		3. DATES COVERED (From - To) April 2010 - Sept 2010	
4. TITLE AND SUBTITLE A Hybrid Kinetic Model of Asymmetric Thin Current Sheets with Sheared Flows in a Collisionless Plasma				5a. CONTRACT NUMBER	
				5b. GRANT NUMBER	
				5c. PROGRAM ELEMENT NUMBER 67-9871-00	
6. AUTHOR(S) James Chen, Robert A. Santoro,* Adam Szabo,** and Davin E. Larson***				5d. PROJECT NUMBER	
				5e. TASK NUMBER	
				5f. WORK UNIT NUMBER	
7. PERFORMING ORGANIZATION NAME(S) AND ADDRESS(ES) Naval Research Laboratory 4555 Overlook Avenue, SW Washington, DC 20375-5320				8. PERFORMING ORGANIZATION REPORT NUMBER NRL/MR/6790--10-9309	
9. SPONSORING / MONITORING AGENCY NAME(S) AND ADDRESS(ES) Office of Naval Research 875 North Randolph Street Arlington, VA 22203-1995				10. SPONSOR / MONITOR'S ACRONYM(S) ONR	
				11. SPONSOR / MONITOR'S REPORT NUMBER(S)	
12. DISTRIBUTION / AVAILABILITY STATEMENT Approved for public release; distribution is unlimited.					
13. SUPPLEMENTARY NOTES *NRC Postdoctoral Research Associate, Naval Research Laboratory, Washington, DC; present address: Aerospace Corporation, 15049 Conference Center Drive, Chantilly, VA **NASA Goddard Space Flight Center, Greenbelt, MD ***Space Science Laboratory, University of California, Berkeley, CA					
14. ABSTRACT A new model of equilibrium current sheets in a collisionless plasma incorporating ion flows that are asymmetric and sheared across the current sheet is developed. Ions are treated as single particles and electrons as a massless fluid. The resulting current sheet is a Vlasov equilibrium satisfying Ampere's law. The current sheet thickness is shown to be of the order of the ion Larmor radius. It is found that the structure of the current sheet depends on the distribution function of the ions entering the current sheet. A characteristic feature of this class of equilibria is that the pressure tensor is anisotropic and nondiagonal while the reversing component of the magnetic field is similar to the hyperbolic tangent Harris field. The results show that the asymmetric sheared ion momentum flows as well as the off-diagonal pressure tensor elements play an essential role in the force balance. The model is applied to current sheets co-moving with the solar wind and is directly compared with high-resolution WIND MFI magnetic field data and WIND 3DP particle data. The agreement is good. The theoretical results are scalable to collisionless plasmas in different regimes.					
15. SUBJECT TERMS Asymmetric Collisionless Current Sheet Solar Wind Theory Reconnection Hybrid Simulation					
16. SECURITY CLASSIFICATION OF:			17. LIMITATION OF ABSTRACT UL	18. NUMBER OF PAGES 43	19a. NAME OF RESPONSIBLE PERSON James Chen
a. REPORT Unclassified	b. ABSTRACT Unclassified	c. THIS PAGE Unclassified			19b. TELEPHONE NUMBER (include area code) (202) 767-3134

Table of Contents

1. Introduction	2
2. Physics of Collisionless Current Sheets	5
3. Asymmetric Current Sheet Model	6
3.1 Coordinate System	7
3.2 Self-Consistent Equilibrium	8
3.3 Contribution of Ions to Equilibrium	9
3.4 Contribution of Electrons to Equilibrium	11
3.5 The Self-Consistent Equilibrium Fields	12
4. Numerical Results	13
5. A Solar Wind Current Sheet	17
5.1 WIND Spacecraft Data	17
5.2 Model-Data Comparison	18
6. Discussion and Conclusions	20
Appendix A	22
Acknowledgments	25
References	25
Figures	29
Figure Captions	40

A Hybrid Kinetic Model of Asymmetric Thin Current Sheets With Sheared Flows in a Collisionless Plasma

James Chen,¹ Robert A. Santoro,^{2,†} Adam Szabo,³ and Davin E. Larson⁴

¹ Plasma Physics Division, Naval Research Laboratory, Washington, DC

² NRC Postdoctoral Research Associate, Naval Research Laboratory, Washington, DC, USA

³ NASA Goddard Space Flight Center, Greenbelt, MD

⁴ Space Science Laboratory, University of California, Berkeley, CA

Abstract

A new model of equilibrium current sheets in a collisionless plasma incorporating ion flows that are asymmetric and sheared across the current sheet is developed. Ions are treated as single particles and electrons as a massless fluid. The resulting current sheet is a Vlasov equilibrium satisfying Ampere's law. The current sheet thickness is shown to be of the order of the ion Larmor radius. It is found that the structure of the current sheet depends on the distribution function of the ions entering the current sheet. A characteristic feature of this class of equilibria is that the pressure tensor is anisotropic and nondiagonal while the reversing component of the magnetic field is similar to the hyperbolic tangent Harris field. The results show that the asymmetric sheared ion momentum flows as well as the off-diagonal pressure tensor elements play an essential role in the force balance. The model is applied to current sheets co-moving with the solar wind and is directly compared with high-resolution WIND MFI magnetic field data and WIND 3DP particle data. The agreement is good. The theoretical results are scalable to collisionless plasmas in different regimes.

Manuscript approved October 21, 2010

[†] Present address: Aerospace Corporation, 15049 Conference Center Drive, Chantilly, VA

1. Introduction

Current sheets occur over a wide range of regimes in solar-system and astrophysical plasmas including the magnetosphere, the solar wind, and the solar corona. Such current sheets can store a significant amount of magnetic energy, and the release of this energy can have important consequences. For example, the disruption of the night-side magnetotail current sheet is thought to cause geomagnetic substorms [e.g., *Dungey*, 1961; *Russell and McPherron*, 1973; *Fairfield*, 1984; *Hones et al.*, 1984]. In the solar and stellar coronae, current sheets are assumed to play an important role in coronal heating [*Parker*, 1984] and solar/stellar flares [*Priest*, 1982]. In laboratory reconnection phenomena, current sheets in confined plasmas have been observed [e.g., *Yamada et al.*, 2000; *Carter et al.*, 2002; *Furno et al.*, 2006; *Lawrence and Gekelman*, 2009].

Perhaps the best understood natural current sheet is the magnetotail current sheet, which has been extensively studied since its discovery [*Ness*, 1965]. The current sheet is observed to become “thin” in association with the occurrence of substorms, characterized by thickness of the order of (several times) the thermal ion Larmor radius based on the field just outside the current sheet [e.g., *Fairfield*, 1984; *Frank et al.*, 1984; *McPherron et al.*, 1987; *McComas et al.*, 1986; *Mitchell et al.*, 1990; *Lui et al.*, 1992; *Sergeev et al.*, 1993; *Asano et al.*, 2003; *Runov et al.*, 2006]. The magnetotail current sheet is embedded in the thicker central plasma sheet. In the solar wind (SW), current sheets are encountered in the form of rotational and tangential discontinuities [e.g., *Lepping and Behannon*, 1986]. Their thicknesses are also of the order of the ion Larmor radius [e.g., *Siscoe et al.*, 1968; *Burlaga et al.*, 1977]. The heliospheric current sheet embedded in a sector boundary may be one order of magnitude thicker than such discontinuities [e.g., *Winterhalter et al.*, 1994]. For the solar corona and astrophysical systems, however, no in situ measurements of current sheets are available.

Current sheets are formed in boundary layers between neighboring regions with oppositely directed magnetic fields. If the regions have nearly the same properties, the current sheets are nearly symmetric. The magnetotail current sheet and the heliospheric current sheet are two such examples. However, current sheets in regions such as the magnetopause, the solar corona, and the solar wind may occur between regions with dissimilar properties. They are expected to be asymmetric. Current sheets have been extensively studied using symmetric geometries, but only limited theoretical understanding of asymmetric current sheets exists at this time. In the present paper, we present results of a study in which a self-consistent asymmetric current sheet equilibrium is constructed using a hybrid (kinetic ion and massless fluid electron) simulation approach, taking into account the exact ion orbits and such properties as the anisotropic and nondiagonal pressure tensor and sheared ion flows.

Figure 1a shows a schematic of a current sheet, with the current in the $+x_2$ direction pointing out of the paper. The normal component $B_3 = B_n = \text{const}$ of the magnetic field is in the direction of x_3 , and the $B_1(x_3)$ component in the x_1 direction reverses direction at $x_3 = 0$. We set $B_2 = 0$ in the present study. The current sheet is represented by the

region between the dashed lines where the curvature of magnetic field “lines” is maximum. We denote the half-width of this region by δ . This geometry is appropriate for a distended dipole field such as the magnetotail and the heliospheric current sheet or for a rotational discontinuity. We will use subscripts 1, 2, and 3 to denote vector components in the x_1 , x_2 , and x_3 directions.

In the solar-system and astrophysical regimes of interest, plasmas are nearly collisionless, i.e., $\nu_i \ll \Omega_i$. Here, ν_i and Ω_i are the characteristic ion collision and Larmor frequencies, respectively. More specifically, the Larmor radius $\rho_n \equiv v_{th}/\Omega_n$ of thermal ions based on B_n and the time ions spend in the current sheet, which is $\sim \Omega_n^{-1}$, are much shorter than the classical mean free path and mean free time, respectively, where v_{th} is the ion thermal speed, $\Omega_n \equiv eB_n/m_i c$, m_i is the ion mass, and c is the speed of light. In these regimes, the structure of a current sheet, whether symmetric or asymmetric, is determined by the collisionless motion of ions, and fluid approximations such as magnetohydrodynamics (MHD) are not applicable.

The particle motion in and the structure of a current sheet can be approximated as one dimensional (1-D) provided $L_{1,2} \gg \rho_n$, where $L_{1,2}$ are the gradient scale lengths along x_1 and x_2 , respectively [Burkhart and Chen, 1993]. With nonzero B_n , the particle motion has only two constants of motion in involution (the Hamiltonian and one canonical momentum) and is nonintegrable even in 1-D [Chen and Palmadesso, 1986]. The charged-particle orbits consist of three distinct classes: transient (sometimes called Speiser-type), stochastic, and integrable (regular) orbits. The transient and stochastic orbits come in from and escape to the asymptotic regions outside the current sheet, defined by $|x_3| \gg \delta$, while the integrable orbits are trapped in the current sheet. In Figure 1a, the asymptotic source regions are indicated by S^+ (for $x_3 \gg +\delta$) and S^- (for $x_3 \ll -\delta$), and the respective incoming particle distribution functions are denoted by f^+ and f^- . The time spent in the current sheet is $\sim \Omega_n^{-1}/2$ for transient orbits and several times Ω_n^{-1} for stochastic orbits. In contrast, the motion in a neutral sheet with $B_n = 0$ is integrable and has no stochastic or transient orbits; all particles in such a neutral sheet remain trapped. This is true with or without a shear component B_2 in the x_2 direction.

As a matter of notation, we will use subscript a to denote quantities defined in the asymptotic regions. Accordingly, $B_a \equiv B_1(|x_3| \gg \delta)$ is the asymptotic value of the reversing field. For current sheets of interest, $B_n/B_a \lesssim 0.5$. Where necessary, we will use superscript $+$ ($-$) to denote quantities defined in S^+ (S^-). Where the distinction is not important, we will use S to denote one or both source regions.

The theoretical understanding to date is mostly based on symmetric current sheets because of their relative simplicity and intrinsic applicability to natural systems such as the magnetotail that are topologically symmetric. In an early theoretical work, Eastwood [1972] studied the properties of 1-D symmetric current sheets having $B_2 = 0$ and $B_n \neq 0$, with incoming particle distributions ($f^+ = f^-$) consisting of cold beams in which all particles have identical field-aligned drift speed v_D at the asymptotic sources. The treatment is self-consistent in that Ampere’s law, $\mathbf{J} = (c/4\pi)\nabla \times \mathbf{B}$, is satisfied. This work was later extended to include thermal spread [Eastwood, 1974] and to current sheets of finite width and length [Eastwood, 1975]. Francfort and Pellat [1976] analytically studied thin current sheets assuming $B_n/B_a \ll 1$ and $v_D/v_{th} \gg 1$ and using an adiabatic invariant of the ion motion [Sonnerup, 1971]. In these studies, only the transient orbits were included. Lemaire and Burlaga [1976] constructed steady-state solutions of Vlasov-Maxwell equa-

tions for 1-D current sheets with $B_n = 0$ and applied them to tangential discontinuities in the SW. In this self-consistent 1-D model, the current sheet is allowed to be asymmetric. With $B_n = 0$, there are three constants of motion in involution, and all trajectories are integrable.

More recent work has improved on the above models by including the full particle dynamics with $B_n \neq 0$ using simulation techniques [Burkhart *et al.*, 1992; Pritchett and Coroniti, 1992, 1995; Holland and Chen, 1993; Harold and Chen, 1996; Hesse *et al.*, 1996] or approximations of particle orbits assuming $B_n/B_a \ll 1$ [Kropotkin *et al.*, 1997; Sitnov *et al.*, 2000]. These works identified the quantity v_D/v_{th} as an important parameter, where v_{th} is the thermal speed of the asymptotic source particle distributions. For the magnetotail, $v_D/v_{th} \ll 1$ is appropriate for quiet-time conditions, while $v_D/v_{th} \gg 1$ corresponds to field-aligned source distribution functions for disturbed situations with strong convection electric fields.

All of the above equilibrium models produce self-consistent magnetic field profiles similar to the hyperbolic tangent Harris field [Harris, 1962], but the plasma properties are noticeably different for the two regimes. In the $v_D/v_{th} \gg 1$ regime [Eastwood, 1972, 1974; Burkhart *et al.*, 1992; Pritchett and Coroniti, 1992; Kropotkin *et al.*, 1997], the particle density is highly peaked in the current sheet, as in the Harris model. In the $v_D/v_{th} \ll 1$ regime, in contrast, the particle density profile is nearly constant across the current sheet [Holland and Chen, 1993; Sitnov *et al.*, 2000]. The latter configuration is consistent with the observed plasma densities in the quiet-time magnetotail current sheet [McComas *et al.*, 1986; Sergeev *et al.*, 1993].

The functional form of the incoming source distribution is also an important parameter. Burkhart *et al.* [1992] used a drifting Maxwellian as a source distribution and found no equilibrium solutions for their simulations in the $v_D/v_{th} \lesssim 1$ regime. In contrast, Holland and Chen [1993] obtained solutions at values as low as $v_D/v_{th} = 0.05$ using a κ -function distribution [Christon *et al.*, 1989], which is prevalent in space plasmas. Physically, the high-energy tail of a κ distribution provides excess particles executing transient orbits relative to a Maxwellian distribution, producing the current that overcomes plasma diamagnetism. Sitnov *et al.* [2000] also found equilibrium solutions in the $v_D/v_{th} \ll 1$ regime assuming $B_n/B_a \ll 1$. In these studies, the pressure tensor was found to be anisotropic and nondiagonal, in contrast to the isotropic and diagonal pressure tensor of the Harris model while $B_1(x_3)$ remained similar to the hyperbolic tangent Harris field. This shows that the Harris-like field can correspond to a range of different particle distribution functions and plasma properties. In comparing models with observations, it is necessary to examine both plasma properties and the magnetic field.

For application to current sheets in the SW, magnetopause, solar and stellar coronae, asymmetry must be allowed. For the SW, two common types of discontinuities have been discussed [e.g., Lepping and Behannon, 1986]: rotational discontinuities (RDs), characterized by $B_n \neq 0$, and tangential discontinuities (TDs), which have $B_n = 0$ at the midplane of discontinuity. The magnetic topology is distinct for the two types of discontinuities, but current sheets are present at field reversals in either case. Our goal here is not to differentiate between the different types of magnetic discontinuities, but rather to focus on the generic properties of collisionless current sheets at magnetic discontinuities.

Lee and Kan [1979] used a method similar to that of Lamaire and Burlaga [1976] and constructed steady-state solutions of the Vlasov-Maxwell equations for the magnetopause

with asymmetry and significant jumps in physical quantities. *Ding et al.* [1992] investigated the dependence of the collisionless tearing mode on the asymmetry of the current sheet. Recently, particle-in-cell (PIC) simulations of collisionless magnetic reconnection in asymmetric current sheets have been carried out [*Swisdak et al.*, 2003; *Pritchett*, 2008]. *Cassak and Shay* [2007] provided a theory and simulation of asymmetric reconnection in the MHD regime. *Malova et al.* [2007] proposed a model of asymmetric thin current sheets using approximate ion dynamics. They injected an ensemble of ions from one side of a current sheet defined by $B_1, B_3 \neq 0$ and $B_2 = 0$ and examined the spatial structure of B_1 , density n , and current J_2 (all expressed in our coordinate system shown in Figure 1b). The magnetic field profile was found to be similar to the hyperbolic tangent Harris field for varying degrees of asymmetry. The self-consistency of the results and the ion flows in the current sheet were not examined. *Mingalev et al.* [2009] extended this work and constructed numerical equilibria satisfying the self-consistent force balance required to a good approximation. In both models, the ion density profiles have pronounced peaks at the field reversal, and the electron contribution to the current is neglected.

In the present paper, we develop a hybrid kinetic model of asymmetric current sheets including the electron contributions, treating ions as kinetic particles and electrons as a massless fluid. We focus on the detailed particle distributions and velocity moments thereof. The model current sheet is self-consistent and is characterized by an anisotropic and nondiagonal pressure tensor as well as asymmetric flows. The calculated current sheet properties will be directly compared with high-resolution solar wind data from the WIND MFI (0.044 sec sampling rate) [*Lepping et al.*, 1995] and WIND 3DP (3-second sampling rate) [*Lin et al.*, 1995] measurements. The agreement is found to be good. The apparent exception is the ion flow speed in the x_2 direction.

As mentioned earlier in connection with the Harris model, the magnetic field profile alone is not sufficient to infer current sheet properties. The SW data show that asymmetric and sheared particle flows across current sheets are correlated with observed magnetic field structures. Thus, any model that attempts to explain current sheets in the SW must simultaneously include asymmetry and sheared flows. In the present work, we extend the self-consistent test-particle model of *Holland and Chen* [1993] by including asymmetry, strongly sheared flows across the current sheet, and an approximate treatment of the electron contribution to the current. The self-consistent test-particle ion approach is the same as that of *Mingalev et al.* [2009] and *Holland and Chen* [1993].

The remainder of this paper is organized as follows. In section 2, we summarize the basic scales governing collisionless current sheets. Section 3 discusses the current sheet model, with the model results given in section 4. In section 5, we compare the numerical results with WIND spacecraft data, and finally, Section 6 gives a discussion of the results along with our conclusions.

2. Physics of Collisionless Current Sheets

The basic physics that determines the structure of collisionless current sheets is the dynamics of the charged particles in the current sheet. In this regard, the existence of distinct classes of orbits corresponding to different phase space regions plays an essential role. In the cold-beam $v_D/v_{th} \gg 1$ regime [*Eastwood*, 1972], where essentially all particles execute identical transient orbits, *Francfort and Pellat* [1976] obtained the scaling for the

half-thickness

$$\delta \sim \left(\frac{v_{th}}{v_D}\right)^{4/3} \rho_a, \quad (1)$$

where $\rho_a \equiv v_{th}/\Omega_a$ is the Larmor radius of thermal ions in the asymptotic field component B_a , and $\Omega_a \equiv eB_a/m_i c$. This expression depends on an approximate adiabatic invariant [Sonnerup, 1971] for transient orbits using the assumption $B_n/B_a \ll 1$ and $v_D/v_{th} \gg 1$. In this regime, we have $\delta \ll \rho_a$ (the “zero-thickness” limit). The scaling was verified for $v_D/v_{th} \gtrsim 1$ by a numerical simulation [Burkhart *et al.*, 1992]. In contrast, in the $v_D/v_{th} \ll 1$ regime, a heuristic derivation [Chen *et al.*, 1990] yielded the scaling

$$\delta \sim \rho_a, \quad (2)$$

in agreement with the results of a more detailed analysis including the nonintegrable motion [Sitnov *et al.*, 2000] and the test-particle simulation of Holland and Chen [1993]. These scaling properties are universal in 1-D in that they only depend on the collisionless ion motion in a current sheet. Note that ρ_a can be related to the ion skin depth λ_i in the asymptotic region by

$$\rho_a = \lambda_i \left(\frac{\beta_a}{2}\right)^{1/2}, \quad (3)$$

where $\lambda_i \equiv c/\omega_{pi}$, $\omega_{pi} = (4\pi n_i e^2/m_i)^{1/2}$ is the ion plasma frequency, and $\beta_a \equiv 2nT/(B_a^2/8\pi)$, assuming $T_e = T_i = T$ for electron and ion temperatures. Here, the Boltzmann constant has been absorbed into T , and we will express temperature in units of energy. For $\beta_a = 1$, we have $\rho_a = \lambda_i/\sqrt{2}$.

The different v_D/v_{th} regimes are determined by the asymptotic source distribution functions, which control the relative population of transient and stochastic particles. Although the particle motion cannot be directly observed, certain observed features such as peaks and valleys in ion velocity distributions obtained in the quiet-time magnetotail [Huang *et al.*, 1989; Holland *et al.*, 1999] can be accurately explained as a direct manifestation of the characteristic phase space resonance exhibited by transient and stochastic orbits [Chen *et al.*, 1990; Burkhart and Chen, 1991; Wang, 1994; Savenkov and Zelenyi, 1996; Holland *et al.*, 1999]. This suggests that the assumption of collisionless particle motion is valid in the magnetotail. The physics scales with the ion Larmor radius, implying that the structure of collisionless current sheets can be scaled from the magnetosphere to the solar wind as well as to laboratory plasmas, where it can be tested against directly measurable plasma and magnetic field data, and ultimately to the solar/stellar coronae. It is the purpose of the present work to (1) understand the structure and (2) test the physics of thin collisionless current sheets in the solar wind.

Note that the usual plasma $\beta \equiv 2nT/(B^2/8\pi)$ is based on the total magnetic field and is of order unity or greater in a current sheet even if the medium has typical $\beta \ll 1$, provided there is no strong “applied” magnetic field due to current distributions outside the current sheet.

3. Asymmetric Current Sheet Model

The model obtains numerical solutions to the steady-state Vlasov-Maxwell equations satisfying $\mathbf{J} = (c/4\pi)\nabla \times \mathbf{B}$. In this approach, the orbits of ions are obtained by integrating

the full equations of motion in electric and magnetic fields and summing the contribution from each ion according to specified input distributions, f^+ and f^- . The model is one-dimensional, having spatial variation only in the direction perpendicular to the plane of the current sheet.

3.1. Coordinate System

Figure 1b shows the coordinate systems used in the analysis. The box represents the current sheet and corresponds to the region of thickness 2δ between the dashed lines in Figure 1a. The x - y - z coordinates are centered at the observer (e.g., the WIND spacecraft) such that the unit vectors \hat{x} , \hat{y} , and \hat{z} are aligned with those of the usual Geocentric Sun-Earth (GSE) coordinates. In this frame, $+x$ points from the Earth to the Sun, $+y$ points out of the page, and $+z$ points northward. The x_1 - x_2 - x_3 coordinate system is defined to be co-moving with the current sheet with the x_3 axis normal to the plane of the current sheet and the x_1 axis parallel to the reversing component of the magnetic field. The dots on the x_1 , x_2 , and x_3 axes are intended to help visualize where the three axes pierce the surfaces of the box facing out of the page at various angles.

Figure 1b depicts the current sheet (thickness 2δ) as moving in the $-x$ direction (to the right) in the x - y - z frame with a velocity V_{SW} . If the structure intercepts the observer on the x axis, the asterisk (*) to the right represents the entry point in the lower surface of the box and the left asterisk the exit point in the upper surface of the box. The distance between the asterisks is always greater than or equal to the actual thickness 2δ and can be much greater depending on angle of inclination of the current sheet to the x - y plane.

The two coordinate systems are related by

$$\mathbf{r} = \mathcal{R}(\mathbf{x} + \mathbf{x}^T) \quad (4)$$

where $\mathbf{x} = (x, y, z)$, $\mathbf{r} = (x_1, x_2, x_3)$, \mathbf{x}^T accounts for the translational motion of the current sheet with respect to the observer, and \mathcal{R} is a matrix specifying rotations in the observer (x - y - z) coordinate system. The vector \mathbf{x}^T is necessary because the observed data are obtained as a time series as the structure advects past the observer at velocity \mathbf{V}_{SW} . Thus, we convert the time series to a function of \mathbf{x} by using

$$\mathbf{x}^T = -\mathbf{V}_{SW}t,$$

where t is time and \mathbf{V}_{SW} is a constant velocity vector chosen to be the SW velocity at the center of the current sheet. The transformation matrix is standard and is given by three successive rotations [Goldstein, 1980]

$$\mathcal{R} = \mathcal{R}_{x''}(\theta_{x''})\mathcal{R}_{z'}(\theta_{z'})\mathcal{R}_y(\theta_y). \quad (5)$$

Here, \mathcal{R}_y is the rotation through angle θ_y about the GSE y axis centered at the observer. The resulting coordinates are denoted by x' , y' , and z' . The operator $\mathcal{R}_{z'}$ is a rotation through $\theta_{z'}$ about the z' axis. The resulting coordinates are x'' , y'' , and z'' . Similarly, $\mathcal{R}_{x''}$ performs a rotation through angle $\theta_{x''}$ about the x'' axis. This yields the desired coordinate system, which is denoted by x_1 , x_2 , and x_3 . We carry out the simulations in the x_1 - x_2 - x_3 coordinates. The observational data are transformed from the GSE into the these coordinates for comparison with the model results.

3.2. Self-Consistent Equilibrium

The model structure is an equilibrium current sheet that is stationary in the x_1 - x_2 - x_3 coordinate system. For simplicity, we assume that the fields are translationally invariant in the x_1 and x_2 coordinates, having variation only in the normal (x_3) direction. This 1-D approximation is valid provided $L_{1,2} \gg \rho_n$, where $L_{1,2}$ are the gradient scale lengths in the x_1 and x_2 directions, respectively.

The equilibrium structure of the current sheet is determined by the motion of ions. The motion and therefore the equilibrium Vlasov distribution functions are functions of the constants of motion. Although the magnetic field is translationally invariant in x_1 and x_2 , the presence of nonzero $B_3 = B_n$ means that the Hamiltonian necessarily depends on x_1 or x_2 in addition to x_3 , rendering the particle motion nonintegrable and chaotic (section 1). We choose a gauge in which the canonical momentum $p_2 = m_i v_2 + q_i A_2(x_1, x_3)/c$ conjugate to x_2 is conserved, where \mathbf{A} is the vector potential.

To start the simulation an initial magnetic field \mathbf{B} and an electric field \mathbf{E} are specified. For simplicity, we assume that the magnetic field is unsheared, i.e., $B_2 = 0$. In the $v_D/v_{th} > 1$ regime, hybrid simulations [e.g., *Pritchett and Coroniti, 1992*] indicate that a nonzero B_2 component in the form of radiating waves is generated. In the $v_D/v_{th} \ll 1$ regime, in contrast, any B_2 component that may arise is small and grows slowly (hundreds of Ω_a^{-1}) [*Cargill et al., 1994*], so that the assumption of unsheared magnetic field is consistent with $v_D/v_{th} \ll 1$. Thus, we take the magnetic field to have the form

$$\mathbf{B}(x_3) = B_1(x_3)\hat{\mathbf{x}}_1 + B_n\hat{\mathbf{x}}_3, \quad (6)$$

where B_n is constant and $\hat{\mathbf{x}}_k$ denotes the unit vector in the x_k direction. With $B_2 = \text{const}$ ($= 0$) and $\partial/\partial x_1 = \partial/\partial x_2 = 0$, the total current density \mathbf{J} is entirely in the x_2 direction,

$$\mathbf{J} = \frac{c}{4\pi} \nabla \times \mathbf{B} = \frac{c}{4\pi} \frac{\partial B_1}{\partial x_3} \hat{\mathbf{x}}_2, \quad (7)$$

with $J_2(x_3) \equiv (c/4\pi)\partial B_1/\partial x_3 = J_{2i}(x_3) + J_{2e}(x_3)$. In the hybrid approach, J_{2i} is calculated using individual ion orbits in order to include the important Larmor radius-scale kinetic effects, while J_{2e} is calculated using the electron fluid equations, taking electron inertia to be negligible on the ion time scales $\sim \Omega_n^{-1}$.

In a 1-D equilibrium, $\nabla \times \mathbf{E} = 0$ implies that E_1 and E_2 are both constant. The component E_3 is determined by Poisson's equation

$$\nabla \cdot \mathbf{E} = \frac{\partial E_3}{\partial x_3} = 4\pi e \delta n, \quad (8)$$

where $\delta n \equiv n_i - n_e$. Because E_3 varies over the current sheet with thickness of the order of ρ_a , it can be shown (Appendix A) that $\delta n/n \sim (V_A/c)^2 \ll 1$, where V_A is the characteristic Alfvén speed. Thus, charge neutrality is valid to lowest order, and with this understanding we use

$$n_i = n_e \equiv n. \quad (9)$$

Note that charge neutrality is not an explicit assumption in this model. Rather it depends on $V_A/c \ll 1$ and the current sheet thickness being ρ_a as determined by the ion motion. In *Lemaire and Burlaga's* model with $B_n = 0$, the scalar potential and charge separation are included, finding charge separation to be extremely small ($\delta n/n \sim 10^{-8}$) in the

$v_D/v_{th} \ll 1$ regime. *Lee and Kan [1979]* assumed quasi-neutrality, neglecting $(V/c)^2 \ll 1$ contributions. In our model, the scalar potential is neglected.

We use an iterative method to compute the self-consistent magnetic field, B_1 , and the corresponding plasma properties of the current sheet. In this algorithm, E_2 and B_n are held fixed, but $B_1(x_3)$ is iterated to self-consistency satisfying Ampere's law, $\mathbf{J} = (c/4\pi)\nabla \times \mathbf{B}$. A uniform E_2 field can be transformed away by a so-called de Hoffman-Teller transformation in the x_1 direction so that the calculation can be done by setting $E_2 = 0$. The de Hoffman-Teller transformation velocity is $V_{dT} \equiv cE_2/B_n$, which then must be added to the calculated V_2 if $E_2 \neq 0$. We will keep E_2 in the formulation for possible generalization to the nonuniform $E_2 \neq 0$ case, but the actual simulation will be done using $E_2 = 0$ everywhere. The component E_1 , which is not affected by the de Hoffman-Teller transformation, is set to zero because of the high electrical conductivity of a collisionless plasma. In the presence of asymmetry, there is generally a net pressure variation across the current sheet, so that there can be a nonzero E_3 component in the current sheet if the pressure tensor is symmetric. If the pressure tensor is allowed to be nondiagonal, however, it is possible to construct self-consistent equilibria with $E_3 = 0$. In the present paper, we limit our consideration to a subclass of equilibria having $E_3 = 0$. A number a general properties and implications pertaining to this simplification are discussed in section 3.5 and Appendix A. Note, however, that the treatment in Appendix A is heuristic. In the following sections, we will discuss in detail our treatment for the ions, electrons, and the computation of the self-consistent fields.

3.3. Contribution of Ions to Equilibrium

The ions are treated as particles. For each iteration of the equilibrium computation, a specified ensemble of ions is injected from the boundaries of the simulation, and the particle trajectories are calculated using the equations of motion

$$\mathbf{v} = \frac{d\mathbf{X}}{dt}$$

$$\frac{d\mathbf{v}}{dt} = \frac{q_i}{m_i} \left[\mathbf{E}(X_3) + \frac{\mathbf{v}}{c} \times \mathbf{B}(X_3) \right], \quad (10)$$

where i indicates the ion species, q_i is the ion charge, m_i is the ion mass, and c is the speed of light. Here and henceforth, we use $\mathbf{X}(t)$ and $\mathbf{v}(t)$ to denote the position and velocity of ions along their trajectories, where t is time (an orbit parameter). The \mathbf{B} and \mathbf{E} fields are held fixed in time during each complete iteration of the equilibrium computation, which starts when the particles are injected into the system, and ends when all the particles have exited from the system.

For each iteration, the contribution of each particle to the first three velocity moments, density $n_i(x_3)$, current density $\mathbf{J}_i(x_3)$, and the energy density tensor $\mathbf{Q}_i(x_3)$, is computed using the particle weighting function $w_i(\mathbf{v}_{in})$ for each particle. The weighting function includes both the values of the asymptotic source density (n_i^\pm) and a velocity space factor which is a function of the particle's initial velocity, \mathbf{v}_{in} , when it is injected into the system.

The particle orbits and the velocity moments are computed on a finite grid rather than being continuous functions, and linear interpolation is used to distribute particle quantities onto the grid. For this purpose, we use the coordinates x_1 , x_2 , and x_3 to represent a finite, discrete set of grid coordinates with uniform grid spacing of Δx . (Note that the equations

of motion are not discretized.) Where multiple species of ions are included, each ion species is represented by M_i particles in the equilibrium simulation, and the j th particle is represented by $N^{(j)}$ discrete orbital points. For the j th particle, these orbital points are sampled at discrete times t_m and denoted by $X_3(t_m)$, where $m = 1, 2, \dots, N^{(j)}$. The sampling time interval, $\Delta t \equiv t_{m+1} - t_m$, is equally spaced. The total contribution to the equilibrium velocity moments at a grid point x_3 is obtained by summing the contributions from all the particles that pass within a grid spacing Δx of x_3 . The contribution of the j th particle of species i to the equilibrium velocity moments is given by

$$\begin{aligned} n_i^{(j)}(x_3) &= \frac{1}{N^{(j)}} \sum_{m=1}^{N^{(j)}} w_i^{(j)}(\mathbf{v}_{in}) d\mathbf{v}_{in} \mathcal{C}(x_3, X_3(t_m)), \\ \mathbf{J}_i^{(j)}(x_3) &= \frac{1}{N^{(j)}} \sum_{m=1}^{N^{(j)}} q_i \mathbf{v} w_i^{(j)}(\mathbf{v}_{in}) d\mathbf{v}_{in} \mathcal{C}(x_3, X_3(t_m)), \\ \mathbf{Q}_i^{(j)}(x_3) &= \frac{1}{N^{(j)}} \sum_{m=1}^{N^{(j)}} m_i \mathbf{v} \mathbf{v} w_i^{(j)}(\mathbf{v}_{in}) d\mathbf{v}_{in} \mathcal{C}(x_3, X_3(t_m)), \end{aligned} \quad (11)$$

where $d\mathbf{v}_{in}$ is the differential volume element in velocity space and \mathbf{Q}_i is a tensor. The scalar function $\mathcal{C}(x_3, X_3(t_m))$ is used to interpolate between the particle positions and the grid cell coordinates, and is given by

$$\begin{aligned} \mathcal{C}(x_3, X_3(t_m)) &= 0, & |x_3 - X_3| \geq \Delta x, \\ \mathcal{C}(x_3, X_3(t_m)) &= \frac{\Delta x - |x_3 - X_3(t_m)|}{\Delta x}, & |x_3 - X_3| < \Delta x. \end{aligned}$$

The equilibrium profiles for the first three moments for each ion species are then calculated by summing over all the particle trajectories for a particular species. Thus, the number density for the i th species is given by:

$$n_i(x_3) = \frac{1}{M_i} \sum_{j=1}^{M_i} n_i^{(j)}(x_3).$$

where M_i is the number of particles representing species i . The total ion current density $\mathbf{J}_i(x_3)$ and energy density tensor $\mathbf{Q}_i(x_3)$ are obtained by analogous summations over j .

From these velocity moments, other quantities such as the equilibrium flow velocity, \mathbf{V}_i and the equilibrium pressure tensor \mathbf{P}_i can be determined as follows:

$$\begin{aligned} \mathbf{V}_i &= \frac{1}{q_i n_i} \mathbf{J}_i, \\ \mathbf{P}_i &= \mathbf{Q}_i - m_i n_i \mathbf{V}_i \mathbf{V}_i. \end{aligned} \quad (12)$$

The ion temperature T_i is then computed from the trace of the ion pressure tensor

$$T_i = \frac{\text{tr}\{\mathbf{P}_i\}}{3n_i}, \quad (13)$$

In the equilibrium current sheet the force balance for each ion species is given by

$$\nabla \cdot (\mathbf{P}_i + m_i n_i \mathbf{V}_i \mathbf{V}_i) - n_i q_i \left(\mathbf{E} + \frac{1}{c} \mathbf{V}_i \times \mathbf{B} \right) = 0, \quad (14)$$

where \mathbf{P}_i is the ion pressure tensor, \mathbf{V}_i is the average velocity, and n_i is the ion number density. The Lorentz force $(\mathbf{E} + \mathbf{V}_i \times \mathbf{B}/c)$ is balanced by kinetic forces $\nabla \cdot (\mathbf{P}_i + m_i n_i \mathbf{V}_i \mathbf{V}_i)$ for each species independently since the effect of collisions between ions of different species are small on the relevant time scale and are neglected.

For a system with multiple ion species, all ion contributions are summed over i . Henceforth, however, we will include only one positive ion species, i.e., protons, and designate all proton quantities by subscript i .

3.4. Contribution of Electrons to Equilibrium

We expect the ion dynamics to determine the basic length scale in the problem, i.e., the thickness of the current sheet, and for this reason (and because it would require much greater computing resources) we do not include the individual electron orbits in the model. The model does, however, include the electron contribution to the net (total) current, treating the electrons as a massless fluid. The electron fluid momentum equation is given by:

$$n_e m_e \frac{d\mathbf{V}_e}{dt} = 0 = -en_e \left(\mathbf{E} + \frac{1}{c} \mathbf{V}_e \times \mathbf{B} \right) - \nabla \cdot \mathbf{P}_e \quad (15)$$

where \mathbf{V}_e is the electron flow velocity, \mathbf{P}_e is the electron pressure tensor, and the electron mass m_e is set to zero. Our treatment of the electrons is similar to the hybrid simulation of *Leroy et al.* [1982], except that their simulation is time dependent while our calculation yields time-independent solutions.

From Ampere's law (7), the 1-D system satisfies $J_3(x_3) = 0$ everywhere. With condition (9), this gives $J_3 = en(V_{3i} - V_{3e}) = 0$ and, therefore, $V_{3i} = V_{3e} \equiv V_3$. Equation (7) also shows that $J_1(x_3) = 0$ for $B_2 = \text{const}$ regardless of the constant value, with the result $V_{1i} = V_{1e} \equiv V_1$. The total current density including the electron contribution is

$$J_2(x_3) = en(V_{2i} - V_{2e}). \quad (16)$$

The electron contribution to the net current is

$$J_{2e} = -enV_{2e},$$

where V_{2e} is determined by the electron momentum equation (15) and $n = n_e$.

The x_3 component of (15) is

$$-en_e \left(E_3 - \frac{1}{c} V_{2e} B_1 \right) - \frac{\partial P_{33e}}{\partial x_3} = 0, \quad (17)$$

and the x_3 component of the steady-state ion momentum equation is obtained from equations (12) and (14):

$$en_i \left(E_3 - \frac{1}{c} V_{2i} B_1 \right) - \frac{\partial Q_{33i}}{\partial x_3} = 0. \quad (18)$$

Eliminating E_3 from equations (17) and (18) and using equation (9), we obtain

$$V_{2i} - V_{2e} = -\frac{c}{enB_1} \left(\frac{\partial Q_{33i}}{\partial x_3} + \frac{\partial P_{33e}}{\partial x_3} \right). \quad (19)$$

For the electron fluid, we use the polytropic equation of state [Krall and Trivelpiece, 1986]

$$\frac{d}{dt} \left(\frac{p}{\rho^\gamma} \right) = 0$$

where $p = nT$ is the scalar fluid pressure, $\rho = mn$ is the mass density, and γ is the polytropic index. Assuming that our electron fluid obeys a similar equation of state, we obtain

$$\frac{d}{dt} (n^{-\gamma_e} p_e) = 0, \quad (20)$$

where γ_e refers to the electron fluid. Here, we have assumed diagonally dominant and nearly isotropic electron pressure tensor so that $P_{33e} = p_e$. This is reasonable on the spatial and temporal scales of ion dynamics because of the much faster electron time scales. In addition, since we assume steady-state ($\partial/\partial t = 0$), we have $d/dt = V_3 \partial/\partial x_3$, and equation (20) becomes

$$\frac{\partial}{\partial x_3} (n^{-\gamma_e} p_e) = 0. \quad (21)$$

Using equations (16), (19), and (21), we obtain the total electric current

$$J_2 = J_{Di} \left[1 + \gamma_e \frac{T_e}{T_i} \left(\frac{1}{n} \frac{\partial n}{\partial x_3} \right) \left(\frac{1}{P_{33i}} \frac{\partial Q_{33i}}{\partial x_3} \right)^{-1} \right], \quad (22)$$

where we have used

$$J_{Di} \equiv -\frac{c}{B_1} \left(\frac{\partial Q_{33i}}{\partial x_3} \right).$$

Here, we recognize J_{Di} as the diamagnetic current determined by the ion motion, and the second term in the square brackets is the electron contribution to the total current. In obtaining equation (22), we have made the approximation $p_e/P_{33i} \approx T_e/T_i$. Thus, the total current J_2 can be determined from the ion quantities if γ_e and T_e/T_i are given.

In the solar wind, the density scale length across the current sheet tends to be comparable to the pressure scale length, and the electron and ion temperatures are also comparable. The (T_e/T_i) factor in equation (22) shows that the electron contribution to the current can be significant. In the quiet-time magnetotail current sheet, on the other hand, we have $T_e/T_i \ll 1$, and the electron contribution is less important.

3.5. The Self-consistent Equilibrium Fields

For each iteration, the total equilibrium current is computed using the ion current J_{Di} and equation (22). In order to obtain a smoother solution and improve the rate of convergence in the numerical algorithm, we average the gradients in equation (22) over the region containing the current sheet, yielding

$$\mathbf{J} = J_{Di} \left(1 + \gamma_e \frac{T_e}{T_i} \left\langle \left(\frac{1}{n} \frac{\partial n}{\partial x_3} \right) \left(\frac{1}{P_{33i}} \frac{\partial Q_{33i}}{\partial x_3} \right)^{-1} \right\rangle_{cs} \right) \hat{\mathbf{x}}_2, \quad (23)$$

where $\langle \dots \rangle_{cs}$ indicates the average over the current sheet. We assume an adiabatic electron fluid and take $\gamma_e = 5/3$. In the actual simulation, we use $J_{Di} = enV_{2i}$ to improve numerical

convergence. This substitution results in a local error of $J_{D_i} - J_{2i} = -cen(E_3/B_1)$. The E_3 component can be obtained from the ion momentum (Appendix A), yielding

$$E_3 = \frac{1}{enB_n} \left[\frac{\partial Q_{31i}}{\partial x_3} B_1 + \frac{\partial Q_{33i}}{\partial x_3} B_3 \right]. \quad (24)$$

This shows that E_3 , which is parallel to B_n , depends on pressure gradients. In Harris-like equilibria, the off-diagonal tensor elements are zero, and an electric field E_3 is necessary to balance the forces in the x_3 direction. In our equilibrium system, where the pressure tensor is allowed to be nondiagonal, force balance can be achieved with the gradients of off-diagonal tensor elements. In our simulation, we specialize to a class of self-consistent equilibria with $E_3 = 0$. In such a system, $(\partial Q_{31i}/\partial x_3)B_1$ balances $(\partial Q_{33i}/\partial x_3)B_3$. In this regard, we note that numerically computed E_3 , with derivatives of Q_{3ki} , tend to be numerically noisy so that setting $E_3 = 0$ allows rapid convergence. We also note that averaged over the current sheet, the two extrema in E_3 nearly cancel, and the net contribution of E_3 to the total current calculation mainly depends on the degree of overall asymmetry in the pressure across the current sheet (Appendix A). This is expected to be small in our case.

Once computed, the total \mathbf{J} is used to calculate the magnetic field \mathbf{B} from Ampere's law $\nabla \times \mathbf{B} = (4\pi/c)\mathbf{J}$. The newly calculated \mathbf{B} is then used as the new prescribed magnetic field for the computation of particle orbits. The procedure is iterated until the difference between magnetic fields of successive iterations is negligible. In practice, we use a relaxation technique in which we mix the old and newly calculated magnetic fields in order to generate a smoother result and minimize overshooting from iteration to iteration. Thus, the magnetic field \mathbf{B} for the equilibrium current sheet is self-consistently determined for an imposed E_2 electric field and particle velocity distributions specified in the boundary regions.

Heretofore, we have formally carried \mathbf{E} to show the general structure of the equations. In the actual calculations, however, we assume that $\mathbf{E} = E_2 \hat{x}_2$ with $E_2 = \text{const}$ and apply a de Hoffman-Teller transformation. That is, the calculations will be performed in the frame in which $E_2 = 0$ everywhere. In the original frame, an $\mathbf{E} \times \mathbf{B}$ translation velocity, $V_{dT} \equiv cE_2/B_n$ is added to the velocity of each particle.

4. Numerical Results

For the initial guess of $B_1(x_3)$, we use equation (6) with the Harris profile,

$$B_1(x_3) = B_{a0} \tanh(x_3/\delta_0) \quad (25)$$

where B_{a0} is the initial value of the asymptotic B_1 field, δ_0 is the initial thickness of the magnetic discontinuity corresponding to the initial half-width of the current sheet.

The $B_1(x_3)$ component of the magnetic field evolves with each iteration of the calculation until convergence of the magnetic field is reached. The scale length of the converged magnetic field discontinuity, $B_1/(\partial B_1/\partial x_3)$, can be quite different from δ_0 . We have found the converged magnetic field $B_1(x_3)$ to be insensitive to both the initial B_{a0} and δ_0 .

The simulation encompasses three regions. The current sheet is centered at $x_3 = 0$ and is located in the central region given by $-L_c < x_3 < L_c$, where $L_c \gg \delta_0$. We typically use L_c which is 10–20 δ_0 . On either side of the central region is an asymptotic source region,

defined by $L_c < x_3 < L_a$ (S^+) and $-L_a < x_3 < -L_c$ (S^-). Thus, the actual simulation is bounded by the outer surfaces of the asymptotic regions, $x_3 = \pm L_a$. For the asymptotic regions, we choose $(L_a - L_c) > 3\rho_a$.

In the simulation, we prescribe two ion distribution functions, f^+ and f^- , and inject particles accordingly at the center of the S^+ and S^- regions. They are then allowed to move into the central region, $-L_c < x_3 < L_c$. The asymptotic regions S are provided to allow the particles to follow their correct dynamics beyond the limits ($x_3 = \pm L_c$) of the central region until they exit the simulation through one of the boundaries at $x_3 = \pm L_a$. Because we inject particles from the asymptotic regions, there are no integrable orbits (trapped particles) except for a small number that may be scattered into the integrable regions [Holland and Chen, 1993] in the numerical computation. A quantitative analysis of the effect of trapped particles, which is not expected to be significant, is beyond the scope of this paper.

For the incoming source distribution functions in the S^+ (S^-) asymptotic region, the average flow speed is specified to be U_1^+ (U_1^-) in the x_1 direction. We use a κ -like initial velocity space distribution [Christon *et al.*, 1989], consistent with observations of SW plasmas [e.g., Gloeckler *et al.*, 1992; Chotoo *et al.*, 1998]. A κ -function is a Maxwellian at low energies, having a power law tail at high energies. Defining $v_*^2 \equiv (v_1 - U_1)^2 + v_2^2 + v_3^2$, we use a κ -like distribution function defined by

$$f(v) = n_0 \exp\left(-\frac{v_*^2}{2v_{th}^2}\right) \quad v < 2v_{th},$$

$$f(v) = n_0 \left(\frac{v_*}{2v_{th}}\right)^{-2\kappa} e^{-2} \quad v \geq 2v_{th},$$
(26)

where n_0 is the density normalization factor and v_{th} is the thermal speed of the Maxwellian. In our study, we will use $\kappa = 5$. It is understood that U_1 , n_0 , and v_{th} are separately defined for S^+ and S^- . Note that U_1 is roughly analogous to the parameter V_D of the symmetric case, which is essentially the specified field-aligned drift velocity in the asymptotic region. For the asymmetric case, however, we have $U_1^+ \neq U_1^-$, and there is no simple parameter that precisely corresponds to v_D . In some cases, such as the example to be considered here, the average of U_1^+ and U_1^- can roughly play the role of v_D .

The particle distribution that can be measured by an observer is the total distribution consisting of the input and output distributions, the latter being determined by the numerical integration of orbits. We define V_{1i}^+ (V_{1i}^-) as the average ion velocity in the x_1 direction of the total particle distribution in asymptotic region S^+ (S^-). The total particle distribution functions in S^\pm also yield other velocity moments such as the ion density n_i^\pm and temperature T_i^\pm .

Let us now consider an illustrative current sheet computation appropriate for a SW plasma near 1 AU. Figure 2 describes a converged equilibrium current sheet obtained by our iterative method. Anticipating comparison of numerical results with SW data, this solution has been obtained to yield the best overall fit to a SW current sheet to be discussed in the next section. From the top, the figure shows the reversing component $B_1(x_3)$, the total (ions plus electrons) current density $J_2(x_3)$, ion density $n_i(x_3)$, and ion temperature $T_i(x_3)$ in the central simulation region, $-L_c < x_3 < L_c$, where we have chosen $L_c = 4000$

km. The B_1 profile can be approximated by a hyperbolic tangent function and resembles the Harris field. The half-width thickness of the converged current sheet is $\delta \simeq 350$ km, which is approximately three times the ion thermal Larmor radius $\rho_a^+ = v_{th}/\Omega_a \simeq 120$ km at $x_3 = L_a$. This confirms the scaling relation (2) and the importance of using a kinetic approach for this problem. The current density $J_2(x_3)$, plotted in the second panel, is highly localized within the central region and shows a characteristic peak at the midplane, with $J_2 \approx 0$ elsewhere. The third panel shows ion density, $n_i(x_3)$, which exhibits an enhancement of about 25% in the current sheet in comparison with the asymptotic value, $n^+ \simeq 3 \text{ cm}^{-3}$, of the converged solution. The ion temperature, given by equation (13), is plotted in the bottom panel. Of particular note is the anti-correlated asymmetry that is present in the temperature and density profiles.

Note that the ion skin depth λ_i for this example is comparable to ρ_a . Using the asymptotic density of the converged solution, $n^+ \simeq 3 \text{ cm}^{-3}$, we obtain $\lambda_i \simeq 130$ km, showing $\rho_a \simeq \lambda_i$. The asymptotic values $B_a^+ \simeq 3.7$ nT and $T_i^+ \simeq 10$ eV yield $\beta_a^+ \simeq 2$, consistent with equation (3). The usual plasma β is defined with the total magnetic field. For the parameters given above, $\beta^+ = 2nT/(B^2/8\pi) \approx 1.6$ in region S^+ for the converged current sheet. At the center of the current sheet where $B_1 = 0$, we have local $\beta \approx 40$.

For this example, the quantity $\langle \dots \rangle_{cs}$ in equation (23) is computed to be $\simeq 0.6$. Using $\gamma_e = 5/3$ and $T_e = T_i$, we find that $J_{2e} \simeq J_{2i}$ so that the electron current accounts for approximately half of the total current J_2 . In the magnetopause model of *Lee and Kan [1979]* where $T_i/T_e \sim 10$, the electron current was found to be about one quarter of the total current.

The asymmetry in $n_i(x_3)$ and $T_i(x_3)$ arises primarily from the asymmetric input source particle densities. Force balance may also require asymmetry in $n_i(x_3)$ and $T_i(x_3)$ if there is asymmetry in the flow velocity. That is, if the directed momentum flow ($n_i m_i \mathbf{V}_i \mathbf{V}_i$ term) is not balanced across the current sheet, an asymmetry in the temperature is required to achieve total force balance.

Figure 3 shows the components of the average ion flow velocity \mathbf{V}_i , obtained as the first-order velocity moment of the total ion distribution function in the simulation current sheet. The $V_{1i}(x_3)$ profile is asymmetric and nonzero. In contrast, in the symmetric case, $V_{1i} \simeq 0$ everywhere [e.g., *Holland and Chen, 1993; Harold and Chen, 1996*]. The asymmetry in the average velocity is mainly due to $U_1^+ \neq U_1^-$. The second panel shows that V_{2i} is highly peaked in the current sheet with $V_{2i} \simeq 0$ elsewhere. Noting the relatively flat $n_i(x_3)$ profile across the current sheet (Figure 2, third panel), we see that it is this sheared $V_{2i}(x_3)$ profile that provides the current sheet current. This is in contrast to the Harris model in which $V_2(x_3)$ is uniform with a peaked $n_i(x_3)$ but is similar to the symmetric case in the $v_D/v_{th} \ll 1$ regime previously studied [*Holland and Chen, 1993*]. The flow velocity for the electrons, V_{2e} , is in the opposite direction as determined by equation (23). The third panel shows V_{3i} , which is perpendicular to the current sheet. Recall from the discussions in section 3.4 that $V_{1i} = V_{1e}$ as well as $V_{3i} = V_{3e}$.

An interesting effect is that the degree of asymmetry in the asymptotic distribution functions alone can affect the current sheet thickness and the total current. This is a nonlocal and purely kinetic effect and is similar to the process (“kinetic thinning”) whereby the current can be enhanced by increasing v_D/v_{th} , or by increasing the field aligned component of the flow velocity of the particle distributions in remote source regions [*Harold and Chen, 1996*].

We now consider the forces acting on the equilibrium current sheet. Recall that by construction, the electron quantities satisfy the electron momentum equation (15). For the ions, all the moments are obtained as averages over individual ion orbits, and they must satisfy equation (14) in all directions. Thus, there must be nonzero $\partial Q_{3ki}/\partial x_3$ for $k = 1, 2$, and 3.

In order to verify that the simulation moments satisfy this equilibrium force balance required by Vlasov equation, we evaluate for the x_k direction P_{3ki} , $m_i n_i V_{3i} V_{ki}$, and the Lorentz force contribution P_{Lk} defined by

$$P_{Lk}(x_3) \equiv -\frac{q_i}{c} \int_{-L_c}^{x_3} n_i(\chi) (\mathbf{V}_i \times \mathbf{B}) \cdot \hat{\mathbf{x}}_k d\chi, \quad (27)$$

where χ is the integration variable and $k = 1, 2, 3$. To test for force balance in the x_k direction, we sum these contributions and define a vector quantity $C_k(x_3)$ by

$$C_k(x_3) \equiv \frac{1}{P_N} [Q_{3ki}(x_3) + P_{Lk}(x_3)], \quad (28)$$

where the normalization factor is defined by

$$P_N = \left(P_{33i} + m_i n_i V_3 V_3 + \frac{B_1^2}{8\pi} \right)_a.$$

This is the asymptotic total (kinetic + magnetic) pressure in the x_3 direction evaluated at $x_3 = -L_c$. The significance of $C_k(x_3)$ is that if the calculated current sheet is a valid solution of Vlasov equation, $C_k(x_3)$ is equal to the integral of the k th component of equation (14) across the current sheet. That is, the simulation current sheet satisfies equilibrium force balance only if $C_k(x_3)$ is a constant function of x_3 for each k .

For the x_1 direction, Figure 4 describes the ion moments directly calculated from individual ion trajectories. All the quantities are normalized to P_N . The top panel gives the P_{31i} element of the ion pressure tensor, which is found to be comparable in magnitude to the directed momentum flux, $m_i n_i V_{3i} V_{1i}$, shown in the second panel. The fact that the two are comparable is a direct result of the strongly sheared flow V_{1i} since this strong shear results in a large change in the directed momentum flow across the current sheet in the x_3 direction comparable to the change in P_{31} . The third panel shows $P_{L1}(x_3) = -(q_i/c) \int_{-L_c}^{x_3} n_i(\chi) V_{2i}(\chi) B_n d\chi$.

The fourth panel shows $C_1(x_3)$ for the x_1 direction. We see that C_1 is nearly constant, showing that forces in the x_1 direction are well balanced due to the nonzero x_3 -gradients in P_{31i} and $m_i n_i V_{3i} V_{1i}$.

For the force balance in the x_2 direction, Figure 5 displays normalized P_{32i} , $m_i n_i V_{3i} V_{2i}$, P_{L2} , and C_2 . The pressures here are relatively small compared with those in the x_1 and x_3 directions. The main point here is that the sum of the normalized for the x_2 direction, $C_2(x_3)$, is constant to a high degree of accuracy, showing that the velocity moments of ion trajectories are in equilibrium in the x_2 direction.

Figure 6 shows normalized P_{33i} , $m_i n_i V_{3i} V_{3i}$, P_{L3} , and C_3 . Comparing this figure to Figures 4 and 5, we see that the pressure due to the flows, $m_i n_i V_{3i} V_{3i}$, plays a lesser role in the force balance along x_3 than in the x_1 and x_2 directions. In the x_3 direction, the plasma pressure P_{33i} (top panel) essentially balances the Lorentz force term P_{L3} (third panel). In the second panel, we expanded the vertical scale to show the slight asymmetry

(solid line). The dashed line is the quantity $n_i(x_3)V_{3i}(x_3)$ (arbitrary units, scaled to fit the plot), which is essentially constant. This means that the continuity equation $\nabla \cdot (n_i \mathbf{V}_i) = 0$ is satisfied. The force balance in the x_3 direction is demonstrated by the essentially constant $C_3(x_3)$ shown in the bottom panel.

Figures 4–6 demonstrate that continuity and force balance for the ions, equation (14), are well satisfied in all directions by the computed current sheet. The off-diagonal elements and their nonzero gradients in x_3 , i.e., $\partial Q_{3ki}/\partial x_3 \neq 0$, are essential for this balance.

5. A Solar Wind Current Sheet

5.1. WIND Spacecraft Data

The above example shows that the full width of collisionless current sheets is expected to scale with the ion Larmor radius, with $\rho_a \sim 100$ km in the solar wind at 1 AU. Advecting at the SW speed of 400 km/s, such current sheets are expected to appear as structures of the order of 1 second in duration. To compare our model results with in situ SW data, we use the high time-resolution (0.044 sec sampling rate) WIND MFI magnetic field data [Lepping *et al.*, 1995] and 3-second WIND 3DP ion data [Lin *et al.*, 1995]. We do not include the high resolution (3 sec) electron data since the electron data are generally not sufficiently accurate for short time scales due to photoelectron contributions, which can only be corrected for by processing the data over longer periods. For this reason we only use the average ratio of the electron to ion temperatures, T_e/T_i , over the entire simulation box as input to the simulation. The WIND MFI magnetic field data have estimated measurement uncertainties of ± 0.1 nT. The major measurement errors in the WIND 3DP particle data are due to truncation errors in processing the digitized data and are typically ± 2 km s⁻¹.

In Figure 7, we show the WIND MFI data for a SW magnetic discontinuity centered, appearing as a sharp reduction in $|B|$, at 16:28:28.5 UT on 1996 January 16. The open diamonds are the 3-second time-averaged WIND MFI data, showing the magnitude of B and its three components in the GSE (x - y - z) coordinates. The magnetic field is actually sampled at 0.044-second time resolution. This is shown by the jagged line overplotted on the 3-second data points. The spin period of the spacecraft is 3 seconds so that the higher-resolution data show noticeable spin effects. The 3-second data shown here have been averaged over the spin period to eliminate these effects. The figure shows that the magnetic discontinuity is now defined by one data point but that the overall width and depth of the magnetic field reduction are not significantly modified by the averaging process. However, the 0.044-second data possibly show a slightly ($\sim 20\%$) narrower width than may be inferred from the 3-second average. Based on the B_x and B_y components, we see that the sharp reduction in B is due to a field reversal, i.e., a current sheet.

Figure 8 shows the magnitude and vector components of the ion flow velocity \mathbf{V}_i as measured by the WIND 3DP instrument. The data are shown in the GSE coordinates. We use the highest time-resolution particle data available, which is 3 seconds for this event. The data indicate that there is a significant amount of shear in the ion flows across the current sheet.

Overall, we find that an asymmetric current sheet is most clearly reflected in anisotropic and nondiagonal pressure tensors and asymmetric ion momentum flows. Such asymmetries are consistent with the recent CLUSTER observations [e.g., Runov *et al.*, 2006]. The

current density J_2 does not show significant spatial asymmetry in the parameter regime studied. Malova et al.'s [2007] model based on approximate ion dynamics also shows only slight spatial asymmetry but did not discuss the properties of the pressure tensor or asymmetric flows.

5.2. Model-Data Comparison

For the purpose of comparing the data with the model results, we transform the 3-second magnetic field data into the coordinate system in which the x_3 axis is normal to the plane of the field reversal, which is calculated using the minimum variance method [Sonnerup and Cahill, 1967]. The transformation is given by equation (5). The specific rotation angles for this SW structure are $(\theta_y, \theta_{z'}, \theta_{x''}) = (-15, 40, 60)$ in degrees. The unit vector normal to the current sheet in the transformed coordinate system is $\hat{x}_3 = 0.408\hat{x} - 0.663\hat{y} + 0.627\hat{z}$ in terms of the GSE unit vectors. The SW velocity is $\mathbf{V}_{SW} = (-550, 23, -15)$ km/sec at the center of the magnetic discontinuity. The same rotation is used to transform the average velocity component V_{ki} . The density and temperature are not affected by this rotation.

From the transformed data we determine the asymptotic values of B_a^\pm , n_i^\pm , V_{1i}^\pm , and T_i^\pm and adjust the input ion distribution functions f^\pm to obtain the solution that has the best overall fit to these boundary values. The specific input parameters to adjust are U_1^\pm , n^\pm , and v_{th}^\pm .

Figure 9 provides a direct comparison of this model current sheet (solid curves) and the 3-second WIND MFI magnetic field data in the transformed frame (open diamonds). Here and in the subsequent plots, observation time is converted to x_3 using the x component of \mathbf{V}_{SW} and the projection of the x coordinate onto the normal to the current sheet. Thus, the 3-second time interval corresponds to the spacing between successive open diamonds. The four panels show that the simulation results are in excellent overall agreement. In particular, the B_1 component (second panel, replotted from Figure 2) clearly shows a hyperbolic tangent-like field and closely fits the observed field reversal. The third and fourth panels show that B_2 and B_3 are both approximately constant, with the values $B_2 \approx 0$ and $B_3 \approx 1$ nT. Thus, the model assumptions regarding the magnetic geometry are well satisfied for this event. The overall agreement between the model and data is good.

The top panel indicates, however, the calculate magnitude of the asymptotic magnetic field is $\sim 15\%$ smaller than the observed values. This is due to the fact that the calculated B_1 is about 15% less than the observed values. This implies that the the total current in the x_2 of the simulated current sheet is less than that of the actual SW structure. While the observed reversal in B_1 is well replicated by the model, the thickness of the reversal region is not well resolved. It is possible that the actual thickness is greater than that of the model field reversal, perhaps by a factor of 1.5 to 2. We did not find a better fit by varying the input parameters given the form of the asymptotic ion distribution function. In the physical system, a slight thickening of the current distribution may occur due to instabilities that can cause diffusion and broadening of the current sheet until nonlinear saturation occurs (e.g. Kelvin-Helmholtz [Miura and Pritchett, 1982; Pritchett and Coroniti, 1984]). Our model does not include such effects.

Figure 10 displays the magnitude and components of the transformed velocity data. Here, the transformed velocity has been \mathbf{V}_{SW} subtracted out so that the data and model

results can be compared directly in a common reference frame. In this figure, we have overplotted the model results (solid curves) shown in Figure 3 on the WIND 3DP data (open diamonds). The top panel shows the magnitude of the velocity, followed by the individual components, V_{1i} , V_{2i} , and V_{3i} . The particle data exhibit more fluctuations than the magnetic field data, but the overall agreement is good with a few notable exceptions.

For V_{1i} (second panel), the jump in V_{1i} from -25 km/sec to 20 km/sec across the magnetic field reversal, the degree and sense of asymmetry, and the near constancy of V_{1i} on either side of the jump are all in good agreement between the model and data. The calculated V_{2i} (third panel) is nearly zero everywhere except around the midplane where it has a pronounced peak. This is in disagreement with data. The observed V_{2i} component is not zero and does not have a simple peak. This discrepancy is greater than the typical error in velocity measurements of the order of ± 2 . The data points exhibit asymmetry across the current sheet, varying from an average of $\langle V_{2i} \rangle \simeq 5$ km/sec for $x_3 < 0$ to $\langle V_{2i} \rangle \simeq 8$ km/sec for $x_3 > 0$. This difference in the measurement values is consistent with the error bars but is probably too systematic to be random fluctuation. The overall deviation from $V_{2i} = 0$ is also greater than the error bars throughout. The most notable difference is the pronounced peak in V_{2i} , which coincides with the dip in the magnitude of velocity $|V_i|$, which arises from the reversal in V_{1i} . The bottom panel of Figure 10 shows a comparison of the calculated V_{3i} component with the observed V_{3i} . Overall agreement in magnitude is again good. In addition, the observed V_{3i} is roughly constant, as is the simulation V_{3i} . The V_{3i} data also exhibits fluctuations of approximately ± 4 km/sec, as in the other components, consistent with but slightly greater than the estimated measurement errors.

In Figure 11 the ion density and temperature profiles for the WIND 3DP data (open diamonds) are compared with the simulation ion density and temperature. The solution is able to approximately (within $\sim 20\%$) match the observed n_i^\pm and T_i^\pm . The model results for both quantities and the data show similar profiles. In particular, the computed n_i jumps from $n_i \approx 2.5$ cm $^{-3}$ to $n_i \approx 3$ cm $^{-3}$ across the current sheet. The observed n_i is nearly constant at 2.5 cm $^{-3}$ for $x_3 < 0$ and increases to 3 cm $^{-3}$ across the current sheet, thereafter slowly decreasing to about 2.7 cm $^{-3}$. The simulated ion temperature and the data exhibit similar asymmetry across the current sheet, but the observed temperature jump, $\Delta T_i \simeq 1$ eV, is smaller than in the model results of $\Delta T_i \simeq 3$ eV. The sharpest jump in temperature occurs on the positive x_3 side of the current sheet in both the data and simulation result. The plasma β of this SW structure is $\beta^+ \approx 1.5$ in S^- and $\beta \approx 30$ in the current sheet.

The calculated velocity components show more discrepancies from the observed data than do other quantities, as described above. The overall offset from zero in the V_{2i} component (third panel, Figure 10) may indicate the presence of an overall drift velocity of about 6 km/s in the observed V_{2i} . Had a constant E_1 component been included in the simulation such that $V_{2E} = cE_1/B_n \approx 6$ km/s, the solution would have been uniformly offset by 6 km/s without significant changes to the equilibrium structure. (A heuristic discussion of the effects of electric field is given in Appendix A.) This would also correspond to nonzero charge separation, which is insignificant for $V_A/c \ll 1$. The presence of a uniform $E_1 \neq 0$, however, would not produce the observed systematic asymmetry in V_{2i} . We also note that the calculated density n_i and temperature T_i profiles (Figure 11) show narrow peaks of about 20% centered at the current sheet, while the data exhibit

no apparent peaks. For both the peaks in n_i and T_i and V_{2i} , the widths are comparable to the 3-second resolution of the instrument. It is possible that the underlying particle feature was not resolved by the 3-second resolution data. Comparing the V_{2i} data in Figure 10 and n_i data in Figure 11, we see that if the observed n_i and V_{2i} truly had no peaks, their product would also have no peak, implying that there would be no ion current sheet. Equation (16) shows that the peak in J_2 on the scale of ρ_a then would all have to come from the electron current J_{2e} . For the simulation parameters, equation (23), with calculated $\langle \dots \rangle_{cs} \approx 0.6$, shows that $J_{2i} \sim J_{2e}$. Thus, it is unlikely that V_{2i} had no peak corresponding to the current sheet, supporting the possibility that the peak was not resolved. Another possibility can be traced to the fact that the width of the observed magnetic discontinuity may be about a factor of two wider than the computed width. If this is true, it implies a wider current peak carrying approximately the same total current, yielding a peak in the measured V_{2i} that is broader and about a factor of two lower in height than what is shown in Figure 10.

We have analyzed several other thin SW current sheets. The model assumptions appear to be well satisfied by the example discussed here. As such it is a good example of the subclass of SW discontinuities with $B_n/B \sim 0.1$, $B_2 \approx 0$, and $\delta \sim \rho_a$. The other examples have the same basic characteristics (e.g., $\delta \sim \rho_a$, asymmetry, peaked J_2 but relatively constant n_i , nondiagonal pressure tensor), but the agreement is not as “clean,” indicating that the model idealization may not be as applicable. Overall, the model describes the other examples with similar degrees of agreement. We have also found examples of magnetic discontinuities whose thicknesses are up to five times thicker in terms of the ion Larmor radius than the examples mentioned here. They may constitute a different class of currents sheets.

6. Discussion and Conclusions

We have presented a model of thin current sheets that occur at magnetic discontinuities in a collisionless plasma. The structure is 1-D but is allowed to be asymmetric about the midplane. The model is valid if the gradient scale lengths in the plane of the current sheet are longer than ρ_n , the Larmor radius in the normal component of the field, B_n and represents a class of self-consistent equilibria in which off-diagonal tensor elements provide force balance with $E_3 = 0$. A hybrid kinetic method is used to numerically obtain time-stationary solutions of the Vlasov-Maxwell equations for specified ion distributions in the asymptotic regions. A κ -like distribution was used as the incoming distribution function for the ions. The current $\mathbf{J}(x_3)$ consists of contributions from both kinetic ions and massless fluid electrons. The scalar potential is neglected, and quasi-neutrality is assumed. The results are self-consistent in that Ampere’s law $\mathbf{J} = (c/4\pi)\nabla \times \mathbf{B}$ is satisfied. Equilibrium force-balance and ion continuity are explicitly verified. In the solar wind at 1 AU, the ion and electron contributions to the current are comparable. All solutions we have obtained converge to thicknesses of a few ion Larmor radii (ρ_a) regardless of the initial choice of B_{a0} and δ_0 , showing a posteriori that a kinetic model including the full ion motion is required. The present model is a significant extension of such past works as that of *Lemaire and Burlaga* [1976], which did not include the nonlinear particle dynamics with $B_n \neq 0$ and that of *Holland and Chen* [1993], which was limited to the symmetric case, both of which excluded strongly sheared flows. As in *Holland and Chen* [1993],

the calculations of *Malova et al.* [2007] and *Mingalev et al.* [2009] also neglect electron dynamics.

The results show that equilibrium current sheet solutions do exist that are (1) asymmetric in the density, current density, flow velocity, and temperature and (2) have strongly sheared flows across the current sheet. We modeled in detail one SW current sheet, for which high-resolution data are available for both the magnetic field and ion. A comparison of the resulting current sheet structure with high-resolution WIND MFI magnetic field and 3DP particle data shows good quantitative agreement, providing a well-constrained test of the model. While we cannot prove that the observed current sheet discussed here is actually in equilibrium, we have shown that the observed properties are consistent with being in equilibrium. We stress that it is crucial to have high-resolution data for both magnetic field and particles for comparison with the model results. This is because different current sheet configurations with different particle properties can have similar magnetic field reversals that can be approximated by the Harris hyperbolic tangent profile. The comparison with the particle data provides critical constraints on the results in terms of matching the flows, density, and temperature.

We have found additional examples of possible axisymmetric current sheets with thickness of the order of ρ_a in the WIND data, but the model fit was not as good as the example discussed in the present paper, with a comparable degree of agreement with the magnetic field data but with worse agreement with the particle data. The data do not have sufficient temporal resolution to identify much thinner current sheets, if any. We did not find any structure identifiable as current sheets having thickness significantly greater than ρ_a .

The conclusion that asymmetric collisionless current sheets are non-Harris-like with strong shears in the average speeds and nondiagonal and anisotropic pressure tensor is important because these plasma properties can strongly influence the stability of such current sheets and play a critical role in the onset of reconnection. For example, pressure anisotropy can strongly affect the collisionless tearing mode [*Chen and Palmadesso*, 1984; *Chen and Lee*, 1985; *Burkhart and Chen*, 1989], modifying the growth rate by more than an order of magnitude in comparison with that for the Harris equilibrium.

Note that a model current sheet is chosen to best fit the boundary values of magnetic field and plasma parameters. The properties of the resulting solution, specifically the thickness and magnitude of the field reversal as well as the degree and sense of asymmetry, are self-consistently determined by the physics of the collisionless ion dynamics and fluid electrons intrinsic to the model.

For the SW current sheets we have examined, only a moderate degree of asymmetry is required. We have also obtained solutions using source distributions f^+ and f^- with much greater degrees of asymmetry. Such solutions tend to have greater shear in the $V_{1i}(x_3)$ component and correspondingly greater current $J_2(x_3)$ than current sheets with less asymmetry and smaller flow velocity. Thus, the degree of asymmetry between the two spatially separated sources remotely affects the structure of the current sheet. This nonlocal effect is analogous to the “kinetic thinning” process in the symmetric case where the current can be enhanced by increasing V_D/v_{th} , or by increasing the field aligned component of the flow velocity of the incoming particle distribution, purely kinetic effect [*Harold and Chen*, 1996].

It is apparent from our sample WIND data that magnetic discontinuities and the associated current sheets in the SW can be thin and that any model that attempts to study these structures must include the ion Larmor-radius scale physics. For both applications to the SW and the magnetosphere, the central physics is the collisionless motion of ions on the spatial and temporal scales of ion gyro motion, with no essential limitation imposed by ambient plasma properties such as magnetic field strength, density, and temperature. The good agreement with the high-resolution WIND data and the previous agreement demonstrated for the magnetotail current sheet suggest that the basic Larmor-radius scale physics underlying our model current sheet is scalable to current sheets in regimes such as the solar and stellar coronae and other astrophysical systems.

Finally, we comment on the electron contribution to the total current. We have treated electrons as a massless fluid under time-stationary conditions and found that the electron and ion contributions are comparable for $T_e \simeq T_i$. In the quiet-time magnetotail where $T_e \ll T_i$, our model would result in $|J_{2e}| \ll |J_{2i}|$ according to equation (23). In this situation, diamagnetic current is dominant. However, under substorm conditions where there is a strong nonuniform and time-varying electric field, it has been noted in numerical simulations [e.g., *Pritchett and Coroniti*, 1995; *Hesse et al.*, 1996] and magnetotail data [*Mitchell et al.*, 1990; *Asano et al.*, 2003] that the electron contribution can dominate the ion contribution. The key difference is that these simulations and observations pertain to driven conditions where significant charge separation may build up in the current sheet, rather than a time-stationary equilibrium scenario. It is interesting to note that even when the electron contribution to the current is dominant, the thickness of the current sheet is still of the order of the ion Larmor radius. The present work shows that the kinetic ion physics plus hybrid electrons yields thin asymmetric current sheets on the scale of ion Larmor radius in agreement with observed SW structures in terms of both magnetic field and particle properties.

Appendix A

In this appendix, we provide a heuristic evaluation of the deviation ($\delta n/n$) from exact charge neutrality due to the asymmetry in the pressure. Equation (8) shows that δn can be approximated by

$$\delta n = \frac{1}{4\pi e} \frac{\partial E_3}{\partial x_3} \sim \frac{E_3^*}{4\pi e \rho_a}, \quad (\text{A1})$$

where the definitions $\delta n \equiv n_i - n_e$ and $\rho_a \equiv v_{th}/\Omega_a$, and $\Omega_a = eB_a/m_i c$ have been used. Here, E_3^* is the maximum value of E_3 , which occurs at $x_3 \simeq \delta/2$, and E_3 is taken to vary over the thickness of $\delta \sim \rho_a$. The E_3 component produces an $\mathbf{E} \times \mathbf{B}$ drift in the x_2 direction in the frame of the current sheet with a characteristic value of

$$V_2^* \equiv c \frac{E_3^*}{B_a},$$

where B_a is the asymptotic value of B_1 as defined in section 1. Using the above equations, we obtain

$$\frac{\delta n}{n} \sim \left(\frac{V_A}{c} \right)^2 \frac{V_2^*}{v_{th}}, \quad (\text{A2})$$

Since $V_A/c \ll 1$ for solar wind conditions and we consider the regime $V_2^* \lesssim v_{th}$ (analogous to $V_D/v_{th} \lesssim 1$, sections 1 and 2), we have

$$\frac{\delta n}{n} \ll 1 \quad (\text{A3})$$

Charge separation is second order in $V_A/c \ll 1$ and is small so that it does not significantly influence the current density profile.

A more precise calculation of δn can be carried out by directly evaluating E_3 . From the ion momentum equation (14), we find

$$\mathbf{E} \cdot \mathbf{B} = \frac{1}{en} (\nabla \cdot \mathbf{Q}_i) \cdot \mathbf{B}. \quad (\text{A4})$$

This yields

$$E_3 = \frac{1}{enB_n} \left[\frac{\partial Q_{31i}}{\partial x_3} B_1 + \frac{\partial Q_{33i}}{\partial x_3} B_3 \right], \quad (\text{A5})$$

where we recall $E_1 = 0$. From equation (28), we see

$$\frac{\partial Q_{3ki}}{\partial x_3} = -\frac{\partial P_{Lk}}{\partial x_3}, \quad (\text{A6})$$

where $k = 1, 2, 4$. This is a general relationship provided the definition (27) is modified to include a nonzero E_3 . For the special subclass of equilibria in which $E_3 = 0$, equations (A5) and (18) yield

$$\frac{\partial Q_{33i}}{\partial x_3} = -\frac{1}{B_n} \frac{\partial Q_{31i}}{\partial x_3} B_1 = -\frac{en}{c} V_{2i} B_1. \quad (\text{A7})$$

The constancy of C_k seen in Figures 4–6 demonstrate that force balance indicated by these relationships is well satisfied in the numerical results.

We have not directly evaluated the right hand side of equation (A5) because of the numerical noise in the derivatives of the elements of \mathbf{Q}_i , but a number of general properties can be rigorously inferred. First, we note that $E_3 = 0$ near the midplane and has two extrema away from the midplane, one negative and one positive at $x_3 \simeq \pm\delta/2$, respectively. This can be seen as follows. For the first term in the square brackets in equation (A5), we have $B_1 \simeq 0$ at $x_3 \simeq 0$ because of the field reversal. The quantity $(\partial Q_{31i}/\partial x_3)$ is peaked in the current sheet because it is the flux of x_1 momentum in the x_3 direction, but because B_1 is essentially an odd function, the product $(\partial Q_{31i}/\partial x_3)B_1$ has two extrema of comparable magnitude and opposite signs. The signs of the extrema depend on the asymptotic distribution functions. In our example, the input particles predominantly enter the simulation region from S^- so that the extrema are negative (positive) for $x_3 < 0$ ($x_3 > 0$). This can be seen from the top two panels of Figure 4. Second, $Q_{33i}(x_3)$ is peaked near $x_3 = 0$ because this is the sum of the plasma and kinetic energy density (equation (12)) so that $\partial Q_{33i}/\partial x_3 \simeq 0$ near the midplane with two extrema of nearly equal magnitude and opposite signs. This is generally true and is also the case for our example, as can be seen from the top two panels of Figure 6. Thus, $E_3 \simeq 0$ near the midplane where the current sheet magnetic field is minimum.

An important implication of the property that $E_3 \simeq 0$ near $x_3 = 0$ is that no significant particle energization due to E_3 is expected near the midplane. Furthermore, the fact that

the extrema have opposite signs means that they tend to cancel when E_3 is integrated over the current sheet so that the net contribution of E_3 to the total current is small unless the degree of asymmetry is sufficiently large.

Equation (A5) shows that in a Harris-like equilibrium where the pressure tensor is diagonal, $Q_{3ki} = 0$ for $k \neq 3$, and an E_3 electric field component is necessary to establish force balance. In contrast, in the class of equilibrium discussed in the present paper, the forces in the x_3 direction are balanced by the off-diagonal tensor elements. This corresponds to a specific set of boundary conditions. It is possible that different equilibrium configurations exist corresponding to different E_3 components determined by the boundary conditions. It is expected that the inclusion of $E_3 \neq 0$ reduces the contribution from the Q_{31i} term. In conjunction with equation (A7), this implies that in general

$$|E_3| \lesssim \frac{V_{2i}}{c} B_1. \quad (\text{A8})$$

This provides an estimate of the maximum value of E_3 , obtained by setting the other contribution to zero. Thus, the $\mathbf{E} \times \mathbf{B}$ drift that results from this field is expected to be $E_3/B_1 \lesssim V_{2i}/c \ll 1$.

Note is that the $\mathbf{E} \times \mathbf{B}$ drift due to E_3 is the same for both the ions and electrons and has no contribution to the total current. This is reflected in the fact that equation (22) contains no contribution from this drift.

In Figure 10 (third panel), the WIND 3DP data does not show a prominent peak in V_{2i} near the midplane of the current sheet while the model result does. The agreement between the data and the model can be improved without significantly modifying the structure of the current sheet if a constant drift velocity V_{2E} of 6 km/sec is added to the simulation results. This would imply a nonzero E_1 field, corresponding to a small amount of charge separation of order $V_{2E}/c \ll 1$.

In a particle-in-cell simulation of magnetic reconnection in an asymmetric current sheet, *Pritchett* [2008] found a strong nonzero electric field in the x_3 direction peaked at the current sheet. This differs from the equilibrium E_3 discussed above. If such a peaked electric field existed in equilibrium, one would expect two oppositely directed peaks in V_{2i} across the midplane of the current sheet, one on each side. The transformed WIND 3DP data for V_{2i} in Figure 10 does not indicate the presence of such features. Comparing with the simulation of *Pritchett* [2008], this indicates that the observed structure was not undergoing reconnection at the time of observation.

There is another $\mathbf{E} \times \mathbf{B}$ drift in the x_2 direction that is produced by the E_1 component. This is distinct from the above drift. In particular, E_1 is constant in a 1-D system (section 3.2) so that this drift is constant. In Figure 10 (third panel), the agreement between the data and the model can be improved without significantly modifying the structure of the current sheet if a constant drift velocity V_{2E} of 6 km/sec is added to the simulation results. This discrepancy may be a manifestation of the effect of a nonzero E_1 field, which is neglected in the present calculation.

Note that the simulations of *Hesse et al.* [1996] and *Pritchett* [2008] show the presence of significant electric fields only during reconnection. The assumption of negligible scalar potential for equilibrium considerations needs to be fully validated in future work but is consistent with these simulation results.

Finally, we note that the constant drift velocity in the Harris model, denoted by V_H , is due to the plasma diamagnetic drift in the x_2 direction. In contrast, the drift velocity discussed here is produced by an electric field. In the Harris model, $\delta = (v_{th}/V_H)\rho_a$, so that $\delta = \rho_a$ when $v_{th} = V_H$. In contrast, the present model yields $\delta = \rho_a$ in the regime $V_{2E} \ll v_{th}$, consistent with the SW data.

Acknowledgments. It is a pleasure to acknowledge many helpful discussions with Dr. J. Krall. We would also like to thank Dr. R. P. Lepping for his help with the WIND MFI data. This work was supported by ONR.

References

- Asano, Y., T. Mukai, M. Hoshino, Y. Saito, H. Hayakawa, and T. Nagai, Evolution of the thin current sheet in a substorm observed by Geotail, *J. Geophys. Res.*, *108*(A5), 1189, doi:10.1029/2002JA009785, 2003.
- Burkhart, G. R., and J. Chen, Collisionless tearing instability of a bi-Maxwellian neutral sheet-An integrodifferential treatment with exact particle orbits *Phys. Fluids*, *B1*, 1578, 1989.
- Burkhart, G.R. and J. Chen, Differential memory in the Earth's magnetotail, *J. Geophys. Res.*, *96*, 14033, 1991.
- Burkhart, G. R., and J. Chen, Particle motion in x -dependent Harris-like magnetotail models, *J. Geophys. Res.*, *98*, 89, 1993.
- Burkhart, G.R., J.F. Drake, P.B. Dusenbery, and T.W. Speiser, A particle model for the magnetotail neutral sheet equilibria, *J. Geophys. Res.*, *97*, 13799, 1992.
- Burlaga, L. F., J. F. Lemaire, and J. M. Turner, Interplanetary current sheets at 1 AU, *J. Geophys. Res.*, *82*, 3191, 1977.
- Cargill, P. J., J. Chen, and J. B. Harold, One-dimensional hybrid simulations of current sheets in the quiet magnetotail, *Geophys. Res. Lett.*, *21*, 2251, 1994.
- Carter, T. A., M. Yamada, H. Ji, R. M. Kulsrud, and F. Trintchouk, Experimental study of lower-hybrid drift turbulence in a reconnecting current sheet, *Phys. Plasmas*, *9*, 3272, 2002.
- Cassak, P. A., and M. A. Shay, Scaling of asymmetric magnetic reconnection: General theory and collisional simulations, *Phys. Plasmas*, *14*, 102114, 2007.
- Chen, J. and Y. C. Lee, Collisionless tearing instability in a non-Maxwellian neutral sheet-An integrodifferential formulation, *Phys. Fluids*, *28*, 2137, 1985.
- Chen, J. and P. J. Palmadesso, Tearing instability in an anisotropic neutral sheet, *Phys. Fluids*, *27*, 1198, 1984.
- Chen, J. and P.J. Palmadesso, Chaos and nonlinear dynamics of single-particle orbits in a magnetotail-like magnetic field, *J. Geophys. Res.*, *91*, 1499, 1986.
- Chen, J., G.R. Burkhart, and C.Y. Huang, Observational signatures of nonlinear magnetotail particle dynamics, *Geophys. Res. Lett.*, *17*, 2237, 1990.
- Chottoo, K., M. R. Collier, A. B. Galvin, D. C. Hamilton, and G. Gloeckler, Extended solar wind helium distribution functions in high-speed streams, *J. Geophys. Res.*, *103*, 17441, 1998.

- Christon, S.P., D.J. Williams, D.G. Mitchell, L.A. Frank and C.Y. Huang, Spectral characteristics of plasma sheet ion and electron populations during undisturbed geomagnetic conditions, *J. Geophys. Res.*, *94*, 13409, 1989.
- Cowley, S.W.H., The effect of pressure anisotropy on the equilibrium structure of magnetic current sheets, *Planet. Space Sci.*, *26*, 1037, 1978.
- Ding, D. Q., L. C. Lee, and D. W. Swift, *J. Geophys. Res.*, *97*, 8453, 1992.
- Dungey, J.W., Interplanetary magnetic fields and auroral zones, *Phys. Rev. Lett.*, *6*, 47, 1961.
- Eastwood, J.W., Consistency of fields and particle motion in 'Speiser' model of the current sheet, *Planet. Space Sci.* *20*, 1555, 1972.
- Eastwood, J.W., Some properties of the current sheet in the geomagnetic tail, *Planet. Space Sci.* *23*, 1, 1975.
- Fairfield, D. H., Magnetotail energy storage and the variability of the magnetotail current sheet, in *Magnetic Reconnection in Space and Laboratory Plasmas*, *Geophys. Monogr. Ser.*, vol. *30*, edited by E. W. Hones, Jr., P. 296, AGU, Washington, D. C., 1984.
- Francfort, P., and R. Pellat, Magnetic merging in collisionless plasmas, *Geophys. Res. Lett.*, *3*, 433, 1976.
- Frank, L.A., C.Y. Huang, and T.E. Eastman, Currents in the Earth's magnetotail, in *Magnetospheric Currents*, edited by T.A. Potemra, p. 147, AGU, Washington, DC, 1984.
- Furno, I., Intrator, T. P., Ryutov, D. D., Abbate, S., Madzima-Nussinov, T., Light, A., Dorf, L., and Lapenta, G., Current-Driven Rotating-Kink Mode in a Plasma Column with a Non-Line-Tied Free End, *Phys. Rev. Lett.*, *97*, 015002, 2006.
- Gloeckler et al., *Astron. Astrophys. Suppl. Ser.* *92*, 267-289, 1992.
- Goldstein, H., *Classical Mechanics*, 2nd ed., p. 147, Addison-Wesley Pub. Co., Reading, Mass., 1980.
- Harold, J. and J. Chen, Kinetic thinning in one-dimensional self-consistent current sheets, *J. Geophys. Res.*, *101*, 24899, 1996.
- Harris, E. G., On a plasma sheath separating regions of oppositely directed magnetic fields, *Nuovo Cimento*, *23*, 115, 1962.
- Hesse, M., D. Winske, M. Kuznetsova, J. Birn, and K. Schindler, Hybrid modeling of the formation of thin current sheets in magnetotail configurations, *J. Geomag. Geoelectr.*, *48*, 749, 1996.
- Holland, D.L. and J. Chen, Self-Consistent current sheet structures in the quiet-time magnetotail, *Geophys. Res. Lett.*, *20*, 1775, 1993.
- Holland, D. L., W. R. Paterson, L. A. Frank, S. Kokubun, and Y. Yamamoto, Signatures of nonlinear charged particle dynamics in Geotail comprehensive plasma instrument observations, *J. Geophys. Res.* *104*, 2470, 1999.
- Hones, E.W., Jr., D.N. Baker, S.J. Bame, W.C. Feldman, J.T. Gosling, D.J. McComas, R.D. Zwickl, J.A. Slavin, E.J. Smith and B.T. Tsurutani, Structure of the magnetotail at $220 R_E$ and its response to geomagnetic activity, *Geophys. Res. Lett.*, *11*, 5, 1984.
- Huang, C. Y., C. K. Goertz, L. A. Frank, and G. Rostoker, Observational determination of the adiabatic index in the quiet time plasma sheet, *Geophys. Res. Lett.*, *16*, 563, 1989.
- Krall, N.A. and A.W. Trivelpiece, *Principles of Plasma Physics*, p. 97, San Francisco Press, San Francisco, CA, 1986.

- Kropotkin, A. P., H. V. Malova, and M. I. Sitnov, Self-consistent structure of a thin anisotropic current sheet, *J. Geophys. Res.*, *102*, 22099, 1997.
- Lawrence, E. E., and Gekelman, W. Identification of a Quasiseparatrix Layer in a Reconnecting Laboratory Magnetoplasma, *Phys. Rev. Lett.*, *103*, 105002, 2009.
- Lee, L.C. and J.R. Kan, A unified kinetic model of the tangential magnetopause structure, *J. Geophys. Res.*, *84*, 6417, 1979.
- Lemaire, J. and L.F. Burlaga, Diamagnetic boundary layers: a kinetic theory, *Astrophysics and Space Science* *45*, 303, 1976.
- Lepping, R.P. and K.W. Behannon, Magnetic field discontinuities: characteristics between 0.46 and 1.0 AU, *J. Geophys. Res.*, *91*, 8725, 1986.
- Lepping, R.P., et al., The WIND magnetic field investigation, *Space Sci. Rev.* *71*, 207, 1995.
- Leroy, M.M., D. Winske, C.C. Goodrich, C.S. Wu, K. Papadopoulos, The structure of perpendicular bow shocks, *J. Geophys. Res.*, *87*, 5081, 1982.
- Lin, R.P., et al., A three-dimensional plasma and energetic particle investigation for the WIND spacecraft, *Space Sci. Rev.* *71*, 125, 1995.
- Lui, A. T. Y., et al., Current disruptions in the near-Earth neutral sheet region, *J. Geophys. Res.*, *97*, 1461, 1992.
- Malova, H. V., L. M. Zelenyi, V. Y. Popov, D. C. Delcourt, A. A. Petrukovich, and A. V. Runov, Asymmetric thin current sheets in the Earth's magnetotail, *Geophys. Res. Lett.*, *34*, L16108, 2007.
- McComas, D. J., C. T. Russell, R. C. Elphic, and S. J. Bame, The near-Earth cross-tail current sheet: Detailed ISEE 1 and 2 case studies, *J. Geophys. Res.*, *91*, 4287, 1986.
- McPherron, R. L., A. Nishida, and C. T. Russell, Is near-Earth current sheet thinning the cause of auroral substorm onset?, in *Quantitative Modeling of Magnetosphere-Ionosphere Coupling Processes*, edited by Y. Kamide and R. A. Wolf, p. 252, Kyoto Sangyo Univ. Kyoto, Japan, 1987.
- Mingalev, O. V., Mingalev, I. V., Malova, Kh. V., Zelenyi, L. M., and Artem'ev, A. V., Asymmetric configurations of a thin current sheet with a constant normal magnetic field component, *Plasma Phys. Reports*, *35*, 76, 2009.
- Mitchell, D. G., D. J. Williams, C. Y. Huang, L. A. Frank, and C. T. Russell, Current carriers in the near-Earth cross-tail current sheet during substorm growth phase, *Geophys. Res. Lett.*, *17*, 583, 1990.
- Miura, A. and P.L. Pritchett, Nonlocal stability analysis of the MHD Kelvin-Helmholtz instability in a compressible plasma, *J. Geophys. Res.*, *87*, 7431, 1982.
- Ness, N.F., The Earth's magnetic tail, *J. Geophys. Res.*, *70*, 2989, 1965.
- Parker, E.N., Magnetic reconnection and magnetic activity, in *Magnetic Reconnection in Space and Laboratory Plasmas*, edited by E.W. Hones, Jr., p. 32, AGU, Washington, DC, 1984.
- Priest, E.R., Magnetic reconnection at the sun, in *Magnetic Reconnection in Space and Laboratory Plasmas*, edited by E.W. Hones, Jr., p. 63, AGU, Washington, DC, 1984.
- Pritchett, P. L., Collisionless magnetic reconnection in an asymmetric current sheet, *J. Geophys. Res.*, *113*, A06210, 2008.
- Pritchett, P.L. and F.V. Coroniti, The collisionless macroscopic Kelvin-Helmholtz instability, 1, transverse electrostatic mode, *J. Geophys. Res.*, *89*, 168, 1984.

- Pritchett, P. L., and F. V. Coroniti, Formation and stability of the self-consistent one-dimensional tail current sheet, *J. Geophys. Res.*, *97*, 16773, 1992.
- Pritchett, P. L., and F. V. Coroniti, Formation of thin current sheets during plasma sheet convection, *J. Geophys. Res.*, *100*, 23551, 1995.
- Runov, A. V., et al., Local structure of the magnetotail current sheet: 2001 Cluster observations, *Ann. Geophys.*, *24*, 247, 2006.
- Russell, C.T. and R.L. McPherron, The magnetotail and substorms, *Space Sci. Rev.* *15*, 205, 1973.
- Savenkov, B. V., and L. M. Zelenyi, Application of separatrix crossing theory to nondiffusion model of current sheet resonance, *Geophys. Res. Lett.*, *23*, 3255, 1996
- Sergeev, V. A., D. G. Mitchell, C. T. Russell, and D. J. Williams, Structure of the tail plasma/current sheet at $\sim 11 R_E$ and its changes in the course of a substorm, *J. Geophys. Res.*, *98*, 17345, 1993.
- Siscoe, G. L., L. Davis, Jr., P. J. Coleman, Jr., E. J. Smith, and D. E. Jones, Power spectra and discontinuities of the interplanetary magnetic field: Mariner 4, *J. Geophys. Res.*, *73*, 61, 1968.
- Sitnov, M.I., L.M. Zelenyi, H.V. Malova, and A.S. Sharma, Thin current sheet embedded within a thicker plasma sheet: self-consistent theory, *J. Geophys. Res.*, *105*, 13029, 2000.
- Sonnerup, B.U.O. and L.J. Cahill, Magnetopause structure and attitude from Explorer 12 observations, *J. Geophys. Res.*, *72*, 171, 1967.
- Sonnerup, B.U.O., Adiabatic particle orbits in a magnetic null sheet, *J. Geophys. Res.*, *76*, 8211, 1971.
- Swisdak, M., B. N. Rogers, J. F. Drake, and M. A. Shay, Diamagnetic suppression of component magnetic reconnection at the magnetopause, *J. Geophys. Res.*, *108*, 1218, 2003.
- Yamada, M., H. Ji, S. Hsu, T. Carter, R. Kulsrud, and F. Trintchouk, Experimental investigation of the neutral sheet profile during magnetic reconnection, *Phys. Plasmas*, *7*, 1781, 2000.
- Wang, Z.-D., Single-particle dynamics of the parabolic field model, *J. Geophys. Res.*, *99*, 5949, 1994.
- Winterhalter, D., E.J. Smith, M.E. Burton, N. Murphy, and D.J. McComas, The Heliospheric Plasma Sheet, *J. Geophys. Res.*, *99*, 6667, 1994.

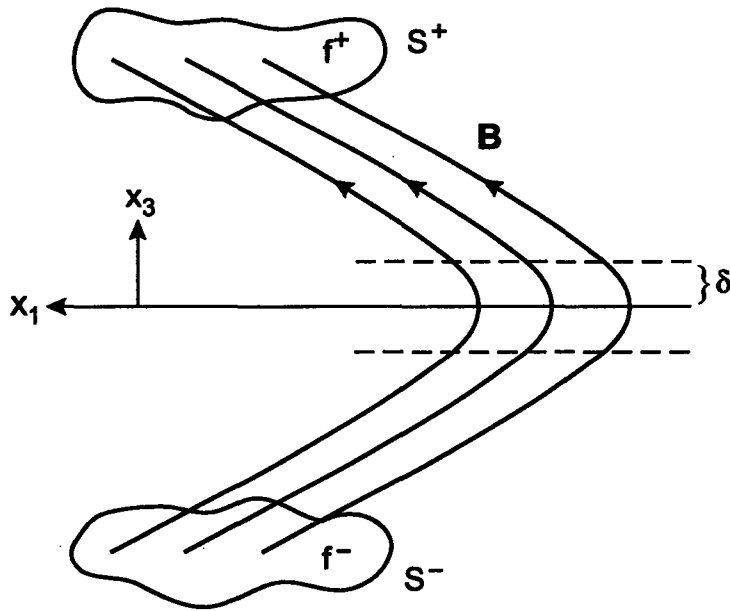


Figure 1a

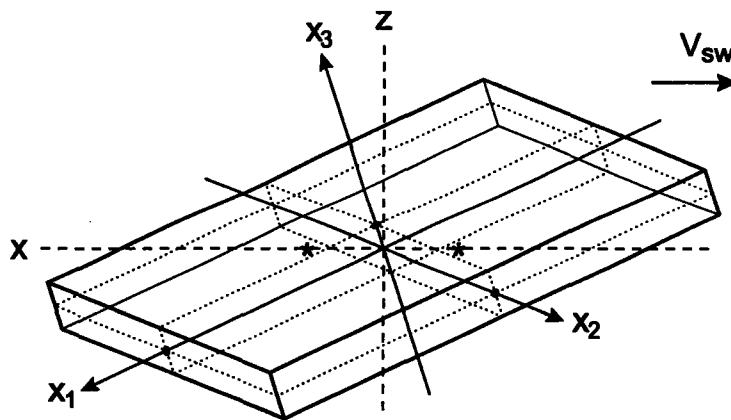


Figure 1b

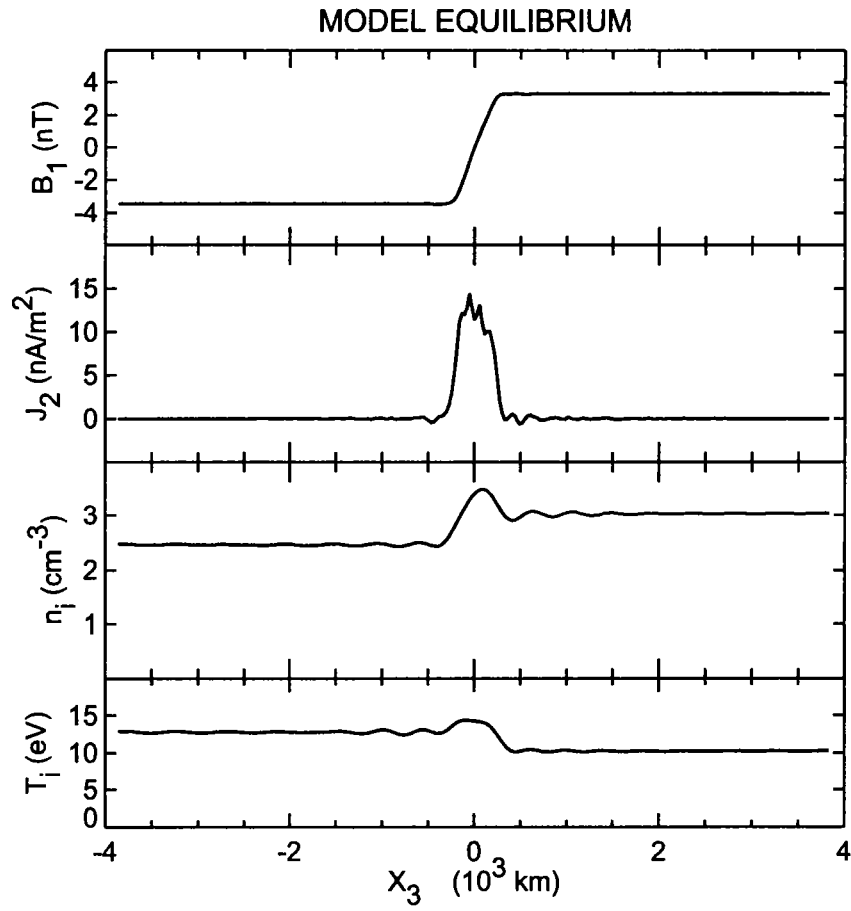


Figure 2

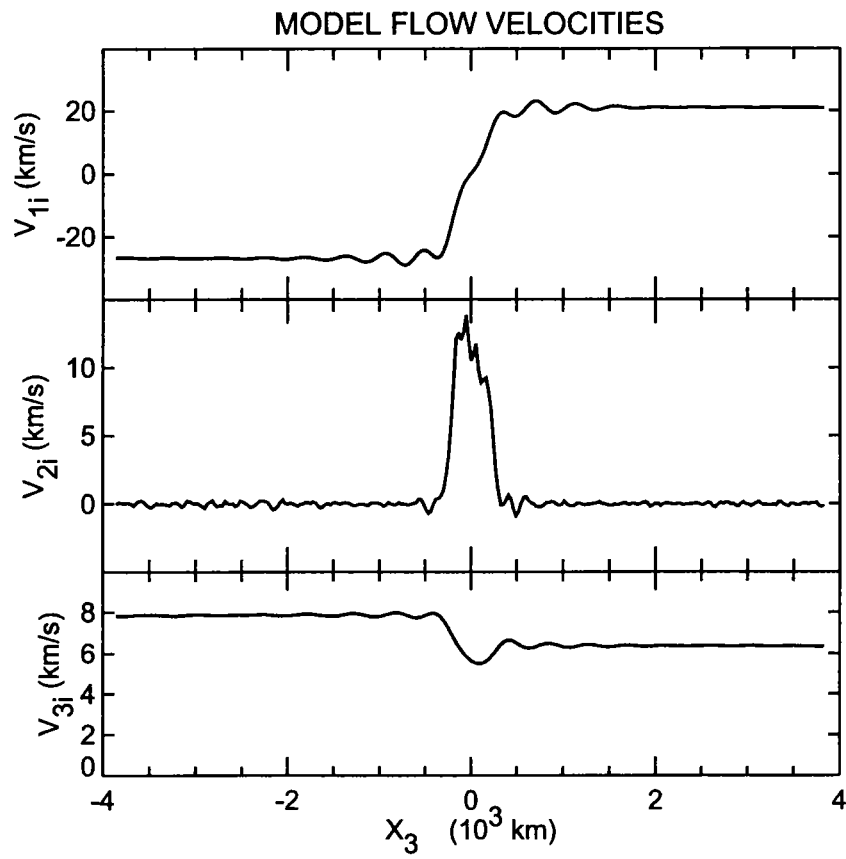


Figure 3

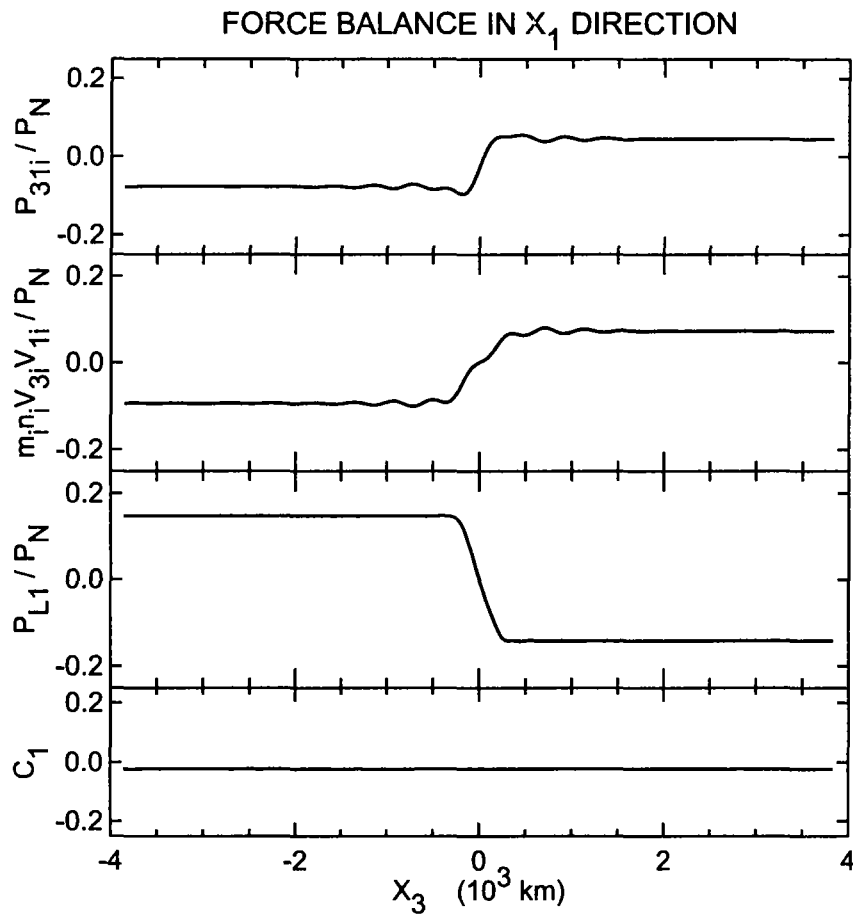


Figure 4

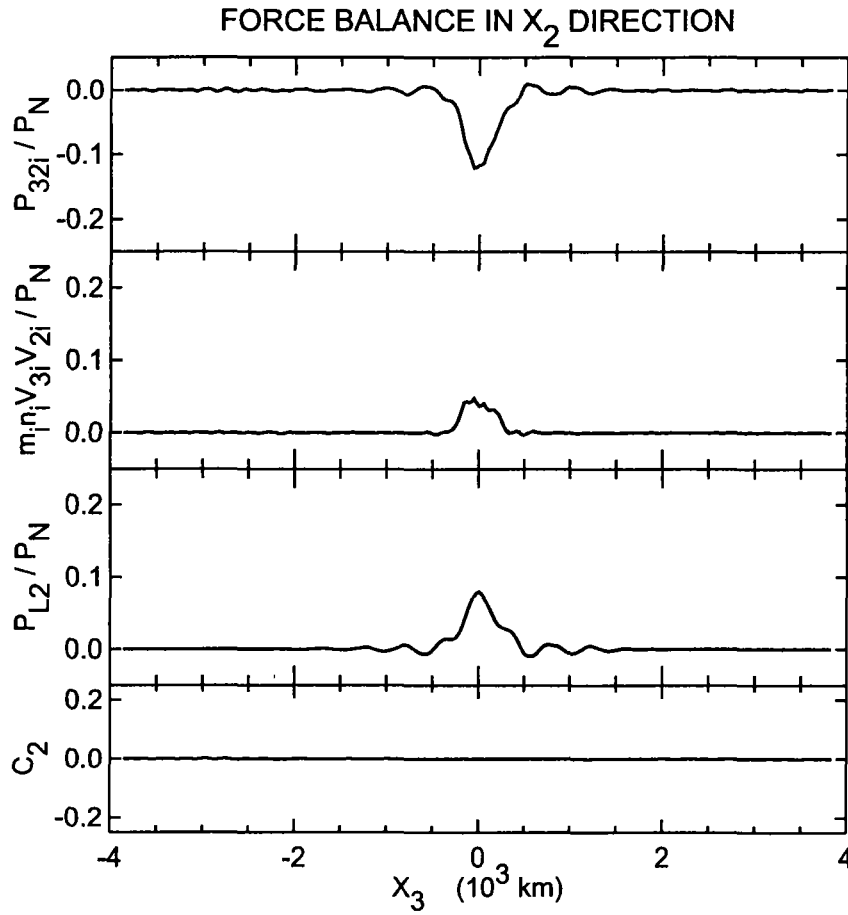


Figure 5

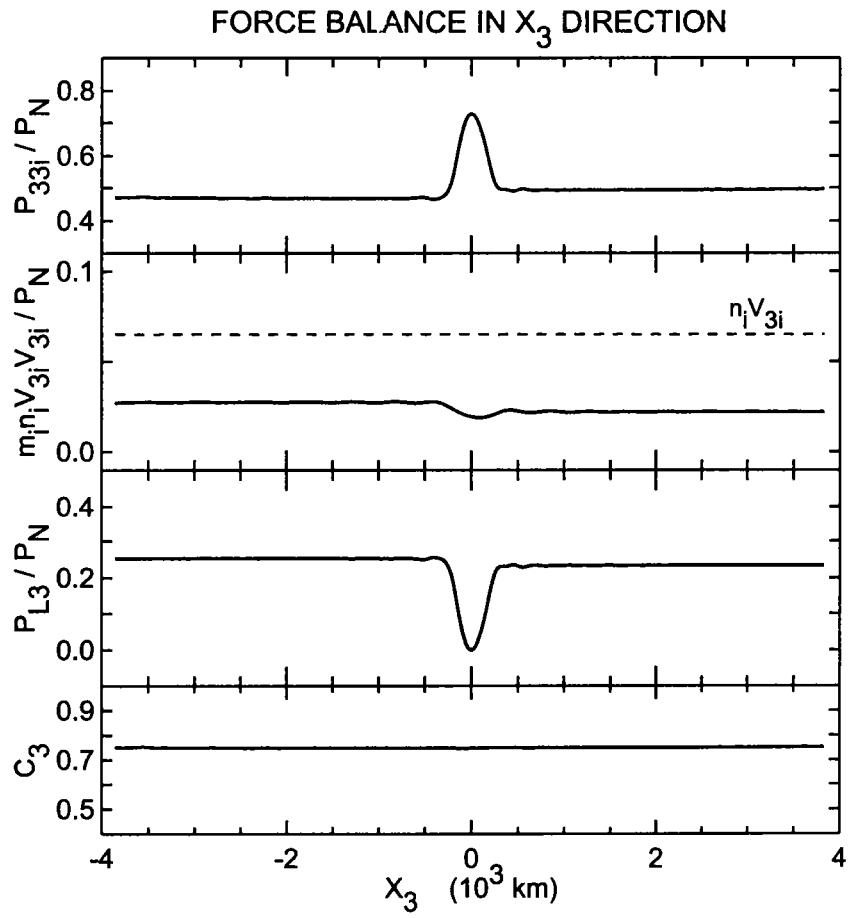


Figure 6

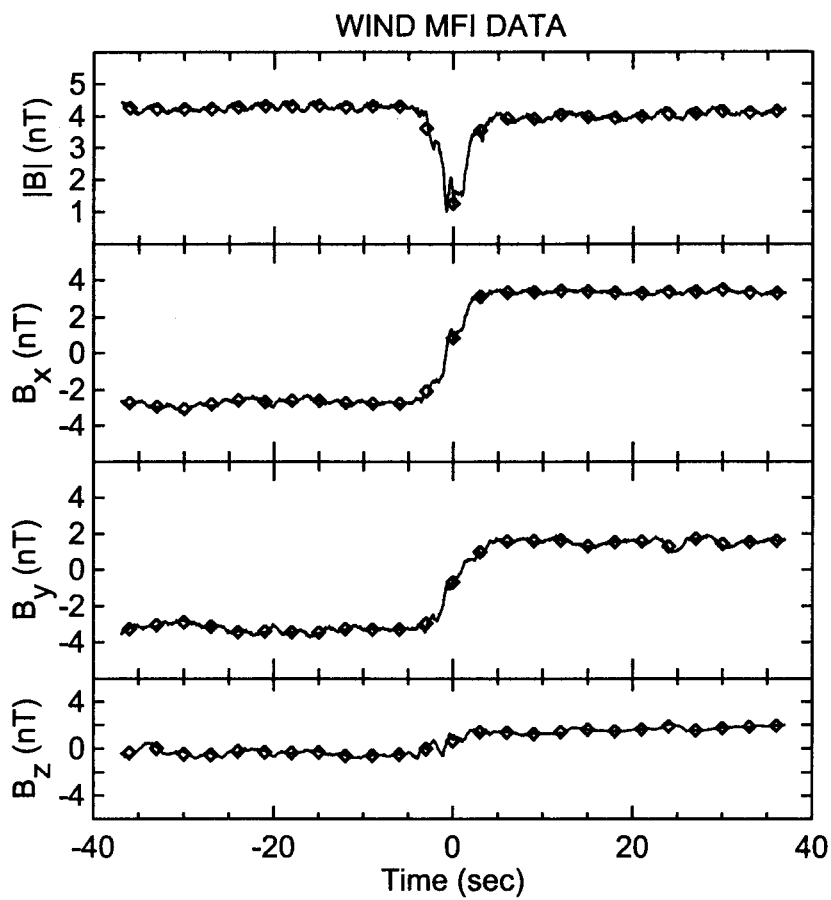
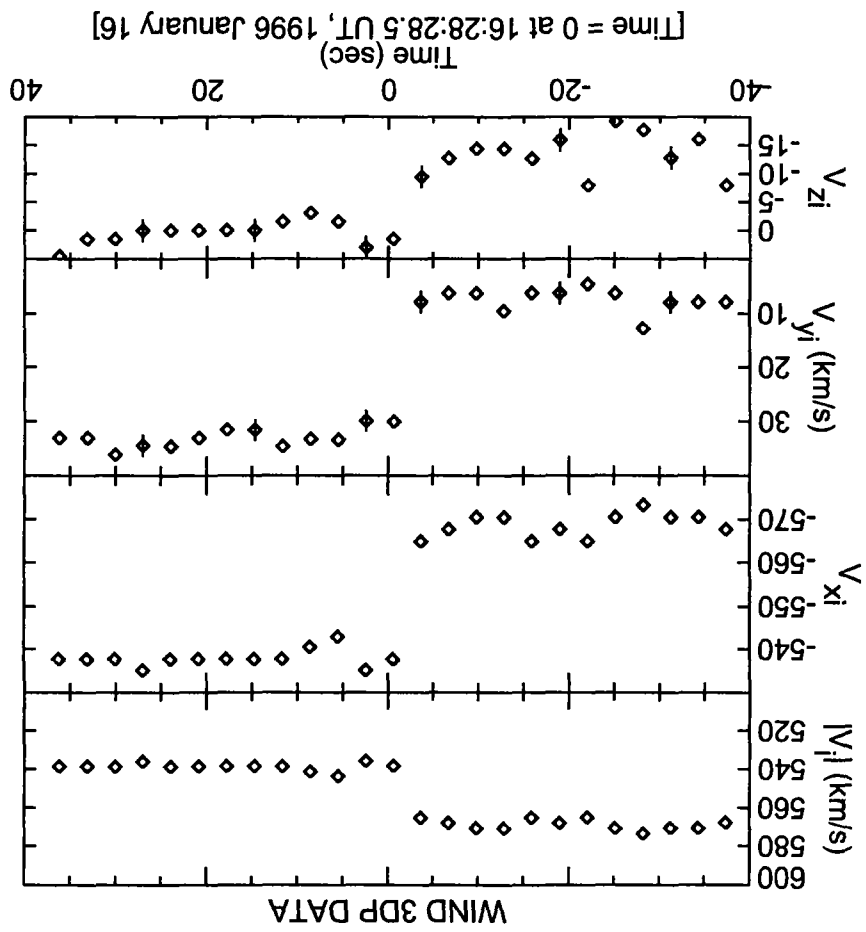


Figure 7

Figure 8



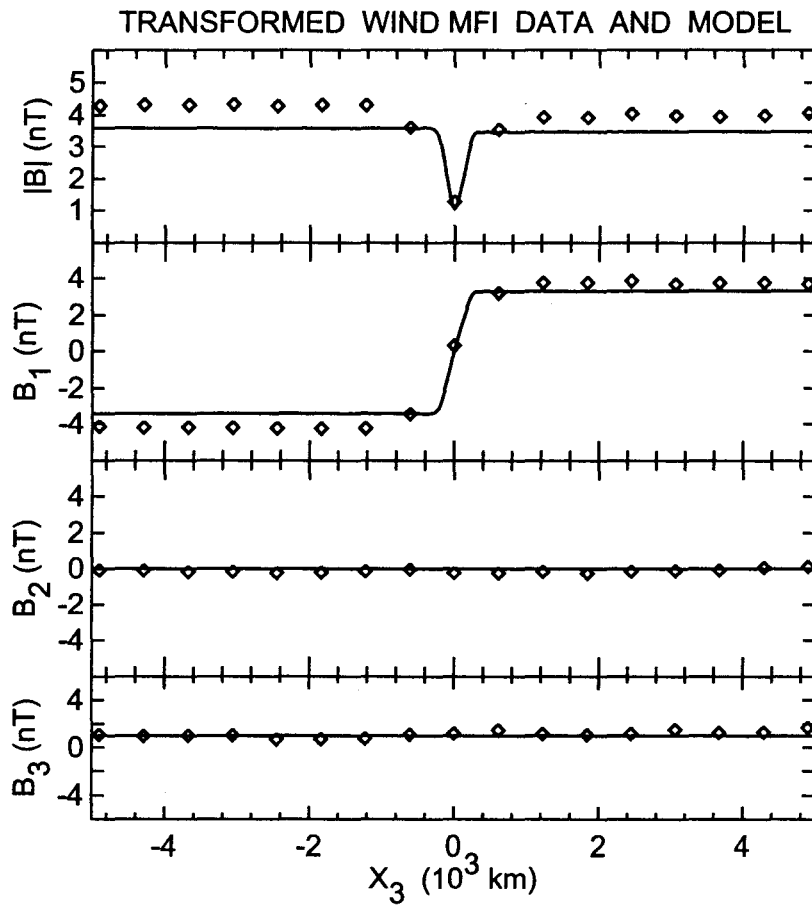


Figure 9

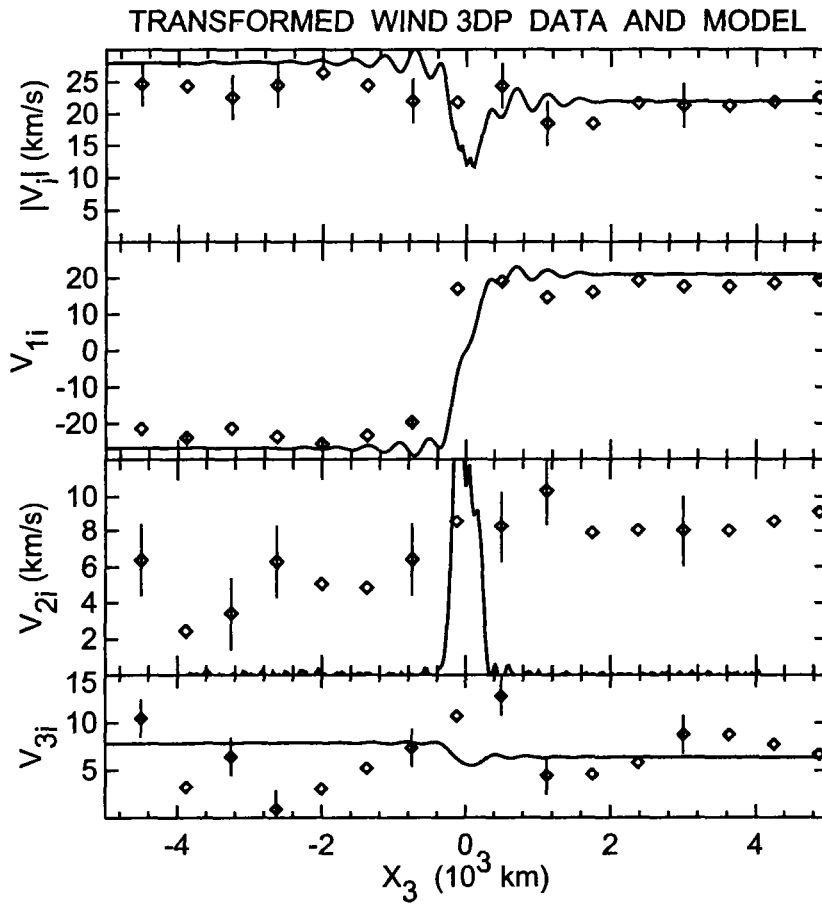


Figure 10

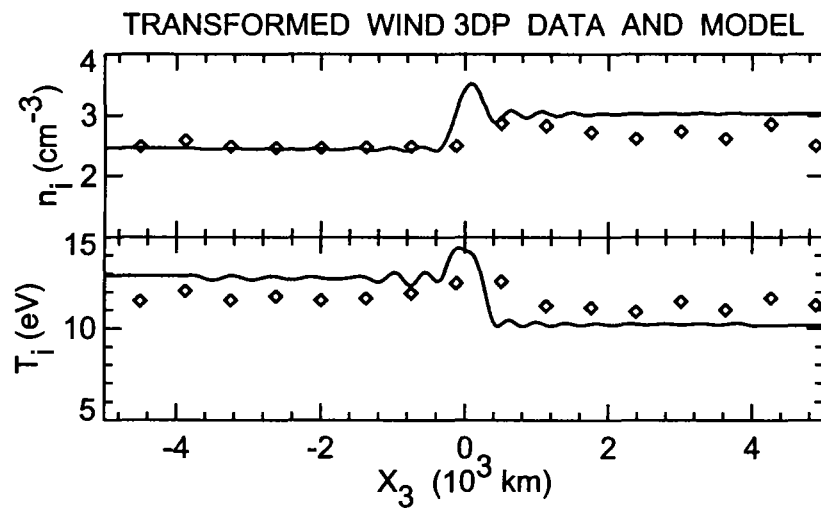


Figure 11

Figure 1. A schematic representation of a current sheet. (a) The current is in the x_2 direction (out of the paper) and is highly peaked between the dashed lines where the “field-line” curvature is maximum. The half-thickness of the current sheet is δ . The two asymptotic regions (S^+ and S^-) far away from the current sheet ($|x_3| \gg \delta$) and the associated particle distribution functions, f^+ and f^- , are shown. (b) Schematic of a current sheet (box) in the solar wind. x , y , and z are aligned with the GSE coordinates, with $+x$ pointing from the Earth toward the Sun, $+y$ out of the page, and $+z$ northward. The x_1 - x_2 - x_3 frame is co-moving with the current sheet, with x_3 perpendicular to the plane of the current sheet. The asterisks (*) represent the entry point (right *, bottom surface) and exit point (* on left, top surface) as the current sheet moves past an observer.

Figure 2. Structure of a self-consistent model current sheet: $B_1(x_3)$ is the magnetic field component in the x_1 direction; $J_2(x_3)$ is the current density in the y_2 direction; $n_i(x_3)$ is the ion density; $T_i(x_3)$ is the ion temperature.

Figure 3. Components of the average ion flow velocity, $V_{1i}(x_3)$, $V_{2i}(x_3)$, $V_{3i}(x_3)$, in the current sheet frame.

Figure 4. Terms in the x_1 component of the ion force equation (14) ($\mathbf{E} = 0$): the pressure, P_{31i} , the momentum flux, $m_i n_i V_{3i} V_{1i}$, and the Lorentz force, P_{L1} (equation (27)), all normalized to P_N . $C_1(x_3)$ is the sum of all contributions. Constant C_1 means that force balance is satisfied.

Figure 5. Terms in the x_2 component of the ion force equation (14) ($\mathbf{E} = 0$): the pressure, P_{32i} , the momentum flux, $m_i n_i V_{3i} V_{2i}$, and the Lorentz force term, P_{L2} (equation (27)), all normalized to P_N . $C_2(x_3)$ is the sum of all contributions. Constant C_2 implies that force balance is satisfied.

Figure 6. Terms in the x_3 component of the ion force equation (14) ($\mathbf{E} = 0$): the pressure, P_{33i} , the momentum flux, $m_i n_i V_{3i} V_{3i}$ (solid), $n_i V_{3i}$ (dashed, arbitrary scale to fit the scale), and the Lorentz force term, P_{L3} (equation (27)), all normalized to P_N . $C_3(x_3)$ is the sum of all contributions. Constant C_3 implies that force balance is satisfied.

Figure 7. WIND MFI data of the magnetic field, \mathbf{B} , in the GSE coordinates, plotted with $t = 0$ at 16:28:28.5 UT, 1996 January 16. The open diamonds show 3 second time-averaged data. The error bars (± 0.1 nT) are approximately the size of the diamonds. The data is sampled at 0.044 sec time resolution is shown by the thin line. The jaggedness arises from the spacecraft spin with a period of 3 seconds.

Figure 8. WIND 3DP data in the GSE coordinates. \mathbf{V}_i is the average velocity for the hydrogen ions. The time axis uses $t = 0$ at 16:28:28.5 UT 1996 January 16. Representative error bars are shown, approximately ± 2 km/sec in each component. For V_i and V_{xi} , the error bars are comparable to the size of the diamonds. The time resolution is 3 seconds.

Figure 9. A comparison of WIND MFI magnetic field data (open diamonds) in the co-moving (x_1 - x_2 - x_3) frame of the current sheet and the simulated equilibrium current sheet (solid curves). The x_3 axis is the minimum variance direction for the data points and is normal to the simulated current sheet. The field reversal occurs in B_1 .

Figure 10. A comparison of WIND 3DP data (open diamonds) for the average flow velocity \mathbf{V}_i of ions and the simulation results (solid curves) in the co-moving frame of the current sheet, as in Figure 9. The V_{1i} component shows a significant amount of flow shear. Representative error bars are shown.

Figure 11. A comparison of WIND 3DP data (open diamonds) for the ion density n_i and temperature T_i and the model results (solid curves) in the co-moving frame of the current sheet, as in Figure 9.